~~Mearusement~~Measurement report: Year-long chemical composition, optical properties, and sources of atmospheric aerosols in the northeastern Tibetan Plateau

Kemei Li[1,3], Yanqing An[1], Jianzhong ~~Xu[1,2]~~Xu[2*], Miao Zhong[1], Wenhui Zhao[1], Xiang Qin[1]

[1]State Key Laboratory of Cryospheric ~~Sciences~~Science and Frozen Soil Engineering, Northwest Institute of Eco-Environment and Resources, Chinese Academy of Sciences, Lanzhou 730000, China
[2]School of Oceanography, Shanghai Jiao Tong University, Shanghai 200030, China
[3]University of Chinese Academy of Sciences, Beijing 100049, China

Corresponding author: Jianzhong Xu (jzxu78@sjtu.edu.cn; jzxu@lzb.ac.cn)

Abstract

~~Due to~~ Brown carbon (BrC) aerosols have attracted considerable attention due to their significant climatic effects, ~~brown carbon (BrC) aerosol has received much attention in recent years.~~yet their sources, optical properties, and seasonal behavior remain poorly understood in remote high-altitude regions. In this study, ~~a~~ year-long fine particular-matter ($PM_{2.5}$) samples were collected at ~~Waliguan Baseline Observatory~~a receptor site in the ~~northeast of the Tibet~~northeastern Tibetan Plateau (TP) to investigate the optical and chemical properties and sources of water-soluble BrC ~~and its source.~~(WS-BrC). The annual average $PM_{2.5}$ concentration ~~of $PM_{2.5}$ throughout the year~~ was 10.3 ± 7.4 μg m^{-3}~~,~~ with ~~maximum in~~ clear seasonal variation (spring ~~(14.0 ± 1.6 μg m^{-3}) and~~ > winter ~~(12.5 ± 1.6 μg m^{-3}) and minimum in~~> fall ~~(7.95 ± 0.9 μg m^{-3}) and~~> summer ~~(7.14 ± 0.9 μg m^{-3}).~~). Organic aerosol (OA) was the major component ~~accounting for~~ across all seasons with an annual contribution of 37.7% ~~on average~~to the total $PM_{2.5}$ mass, followed by sulfate (21.3%), nitrate (12.1%), and other species. ~~OA and nitrate peaked during winter, while sulfate increased significantly during summer.~~ Backward trajectory analysis ~~on air mass reveals~~indicated that ~~the sources of the polluted air mass~~aerosols were mainly transported from the northeast and east of the sampling site. ~~The seasonally average carbon based~~The seasonal mass absorption efficiency ~~(MAE)~~ of WS-BrC at the wavelength of 365nm (MAE_{365}) were 0.92 ± 0.54 ~~Mm~~m^2g^{-1} in spring, 0.40 ± 0.24 ~~Mm~~m^2g^{-1} in summer, 0.81 ± 0.46 ~~Mm~~m^2g^{-1} in fall, and 0.97 ± 0.49 ~~Mm~~m^2g^{-1} in winter, ~~respectively. Comparison with other results, BrC in this study is weakly absorbed~~exhibiting a relatively weak light absorption throughout the year~~,~~ with ~~that during the summer being the most~~the strongest photobleaching in summer. Notably, WS-BrC~~. The chemical compositions~~ light absorption was positively correlated with the oxidation degree of OA during spring and winter, but negatively correlated in summer and fall, suggesting different chemical aging processes and sources of BrC ~~are further investigated by parallel factorization analysis on the three-dimensional excitation-emission matrix and positive matrix factorization analysis on OA~~. These findings enhance our understanding of BrC behavior on the TP and contribute to assessments of its climatic impacts in this high-altitude region.

1 Introduction

Aerosols, ~~tiny~~which are fine particulate ~~matters~~matter suspended in the atmosphere, ~~are~~represent a critical component of climate forcing~~ factor, such as~~, particularly through their effects on atmospheric radiation balance and the ~~water~~hydrological cycle (Forster et al., 2021). ~~Crucially, the influence~~The climatic impacts of aerosols ~~on climate is dictated~~are strongly governed by their physical and chemical properties, ~~including~~such as mass concentration, number concentration, and chemical composition, which ~~vary widely~~exhibit substantially spatial and ~~unpredictably. This variability makes~~temporal variabilities. During atmospheric transport, aerosol undergo extensive physicochemical transformations driven by environmental factors such as relative humidity, oxidants, and solar radiation (Lee et al., 2008; Chen and Torres, 2009; Yu et al., 2022; Klodt et al., 2023). These transformation processes are further influenced by complex topography, which can mitigate the formation and evolution of aerosol characteristics (Schnitzler and Abbatt, 2018; Schnitzler et al., 2022; Fan et al., 2024). These complexities make in-situ ~~measurements~~measurement essential for accurately assessing their impact~~. This is~~, especially ~~important for~~in remote regions where aerosol loading is extremely low~~ and strongly interacted with ambient conditions during transport. For example, during long-range transport, aerosols can interact with gas-phase pollutants like nitrogen oxides (NO_x) and volatile organic compounds (VOCs), which can initiate photochemical reactions leading to the formation of secondary aerosols (Schnitzler and Abbatt, 2018; Fan et al., 2024). These transformations are further influenced by topographic and meteorological conditions that can mitigate the formation and evolution of aerosol characteristics including aerosols' optical properties (Schnitzler et al., 2022).~~.

Aerosol optical properties are key parameters for evaluating their climatic effect. ~~Brown~~Among these, brown Carbon (BrC) and Black Carbon (BC) ~~represent~~are two key optically sensitive components. BrC is particularly notable for its strong wavelength-dependent light absorption properties, ~~distinct~~which is distinguished from the more uniform absorption characteristics of BC (Laskin et al., 2015). ~~Originating from a variety of both anthropogenic and natural sources, BrC contributes significantly to the complexity of aerosol interactions within the atmosphere and remine the major uncertainty of aerosol light absorption estimation~~ Recent studies on BrC have primarily

concentrated on its sources, secondary formation pathways, optical properties, and radiative forcing effects (~~Laskin~~Ma et al., ~~2015; Yan~~2018; Chelluboyina et al., ~~2018~~2024)~~.~~. BrC originates from a wide range of both anthropogenic and natural sources and contributes significantly to the complexity of aerosol-radiation interactions (Laskin et al., 2015; Yan et al., 2018). Field and laboratory studies have revealed important transformations of BrC during atmospheric processes. For example, BrC can undergo photobleaching and oxidative whitening during long-range transport, leading to significantly reductions in its light absorption capacity (Sumlin et al., 2017). In addition, secondary BrC formed through photochemical reactions exhibit distinct diurnal variability: enhanced light absorption in the morning due to active formation processes, followed by significant photobleaching under stronger oxidative conditions in the afternoon (Wang et al., 2019). Furthermore, recent work by Zhong et al. (2023) suggests that light absorption and fluorescence characteristics of BrC are influenced by environmental acidity, indicating the pH conditions may also modulate its optical behavior.

The Tibetan Plateau (TP~~) is~~), the highest and largest plateau on Earth~~. Aerosols in this~~, serves as a key receptor region ~~mainly undergo~~for aerosols transported over long~~-range transport~~ distances from ~~the~~surrounding source ~~region. Recent studies found that WS-~~areas. BrC ~~absorptivity~~light absoption in this cold and remote ~~and cold~~ region ~~has~~exhibits a longer half-life ~~than those in~~ compared to low~~-~~altitude regions, largely due to their ~~lower~~slower decay~~-~~ rate during transport (Choudhary et al., 2022). ~~The higher~~Elevated aerosol ~~loading~~loadings and ~~contribution of~~ BrC ~~on~~contributions are mainly observed along the margins of the TP ~~mainly locates its margin~~ due to the short distance from the source regions (Xu et al., 2024b)~~. Qilian Mountains (QLM), situated on the northeastern margin of the TP represent a background region of inland of China. The importance of this region is represented by its crucial hydrological resource for the arid northwestern region, which is essential for the sustenance of downstream communities and the ecological balance (Chen and Wang, 2009; Liu et al., 2017; Li et al., 2019). Precipitation in the mountain areas, through aerosol-cloud interaction, is the major origination (Qi et al., 2022).~~. In these marginal areas, BrC has been identified as a notable warming agent (Zhu et al., 2024). For example, BrC presented a higher absorption contribution compared to BC in the remote northeastern and southwestern

margins of the TP (Zhu et al., 2021). The Qilian Mountains (QLM), situated on the northeastern edge of the TP, represent a background area of inland China. This region is of hydrological importance, serving as a critical water source for the arid northwestern areas and playing an essential role in sustaining downstream ecosystems and human settlements ~~Xu et al. (2024a)~~(Chen and Wang, 2009; Liu et al., 2017; Li et al., 2019) ~~emphasize the anthropogenic emission from the inland of China significantly increase the concentration of cloud condensation nuclei (CCN) in the QLM. However, the physical and chemical properties of aerosol in this background region is limited understood.~~

. Orographic clouds dominate precipitation generation in the mountainous region (Qi et al., 2022) and aerosol-cloud interactions have become an increasing focus in the QLM (Liu et al., 2019; Xu et al., 2024a) . However, the physical and chemical properties of aerosol in this background region remain poorly understood.

Research ~~focusing aerosol~~on aerosols in the QLM has ~~been~~ aroused ~~increased interesting~~increasing attention during the last ten years (Che et al., 2011; Zhao et al., 2012; Zheng et al., 2015; Dai et al., 2021; Xie et al., 2022). ~~It was found that inorganic~~Inorganic components, especially for sulfate, ~~accounted~~were found to account for a ~~large~~substantial proportion ~~in the~~of aerosol ~~of QLM~~mass (Xu et al., 2014; Xu et al., 2015; Zhang et al., 2019; Zhang et al., 2020). Moreover, organic aerosol (OA) constitutes a significant fraction of the aerosol mass and exhibits significant ~~chemical aging~~aged properties (Zhang et al., 2019; Zhang et al., 2020). Aerosol concentrations in the QLM exhibit a notable seasonal ~~variation~~variability. In spring, the QLM is predominantly affected by the prevalence of mineral dust, while during summer, the region experiences an influence of polluted air masses~~, which are conveyed~~ originating from the northern and northeastern sectors of the ~~TP~~QLM (Xu et al., 2013). However, most previous studies ~~at~~conducted in the QLM ~~are either~~have been short-term or ~~discontinuous which are~~spatially and temporally limited, making it difficult to represent the whole picture of aerosol properties in this region.~~–~~

~~Located in the southeastern edge of the QLM, Waliguan Baseline Observatory (WLG) stands as a~~

~~pivotal research site for understanding the atmospheric environmental variations both locally and regionally. To gain a deeper insight into the effects of human activities on aerosol in this region,~~In this study~~ conducted,~~ a year-long aerosol observation ~~of aerosols at WLG~~ was conducted at Waliguan Baseline Observatory (WLG), located on the southeastern edge of the QLM, to ~~obtain~~investigate the chemical composition, optical characteristics, seasonal variations, and sources of atmospheric aerosols. The primary objective is to enhance understanding of the optical properties of BrC aerosols at a regional scale, and to gain a deeper insight into the influence of chemical processes and sources on BrC in this region.

2 Sample collection and analysis

2.1 Sampling site

The WLG (36°~~170'N~~17′N, 100°~~540'E; 3816m~~54′ E; 3816 m a.s.l.) ~~located~~is situated at the ~~top~~summit of the Waliguan Mountain ~~in~~on the northeastern TP~~, which~~ and is ~~belong to~~part of the Global Atmosphere Watch (GAW) program ~~of~~operated by the World Meteorological Organization (WMO) (Figure 1). The Waliguan Mountain, with a relative elevation difference of about 600m above the ~~ground~~surrounding terrain (Figure 1b), is an ideal location for studying the background characteristics of the atmospheric environment ~~of~~over inner Asia. The WLG is about 90km west of Xining, the capital of Qinghai Province with an elevation of ~2300 m a.s.l. The regional climate ~~at this region~~ is ~~dominated~~characterized by ~~a~~ distinct ~~plateau continental climate, marked~~seasonal variations, strongly influenced by ~~pronounced~~the Asian summer monsoon ~~weather during summer~~ and East Asian winter monsoon ~~during winter~~. Spring and fall serve as transitional seasons between these two climatic systems.

2.2 Aerosol sampling

Fine particulate matter ($PM_{2.5}$) filter samples ~~was~~were collected on 47mm diameter quartz ~~filter~~fiber filters (PALL Life Sciences, USA) using a low flow aerosol sampler (Wuhan Tianhong Instrument Co. LTD, TH-16E) operating at a flow rate of 16.7 L~~.~~ min^{-1}. Before sampling, the ~~quartz~~ filters were baked in a ~~Muffle oven~~muffle furnace at 550°C for ~~4h~~4 hours to remove ~~the carbonaceous~~residual

organic material. After ~~the~~ sampling, each filter was stored in a clean filter ~~box packaged with clean~~ holder wrapped in aluminum foil~~. Subsequently, the box was saved in a ziplock bag~~ and stored at –18°C. A total of 48 filter samples and three ~~blank samples~~field blanks were collected ~~during~~from 14 June ~~14,~~ 2019 ~~and~~to 6 May ~~6,~~ 2020. Each sample was collected for ~~48h~~48 hours with a sampling frequency of once every seven days. ~~The blank filters~~ Field blanks were obtained by ~~being placed in~~ placing clean filters into the sampler for ~~10min~~10-min without ~~pumping. In this study, we divided~~ air flow. For seasonal analysis, the sampling period ~~into different seasons~~ was divided as follows: summer (6 June~~, 2019~~ to 28 August~~,~~ 2019, n = 12), fall (4 September~~, 2019~~ to 27 November~~,~~ 2019, n = 13), winter (11 December~~,~~ 2019 to 26 February~~,~~ 2020, n = 13), and spring (4 March~~, 2020~~ to 6 May~~,~~ 2020~~). The real-time meteorology~~, n = 10). Meteorological data monitored by a Vantage Pro2 (Davis Instruments Corp., Hayward, CA, USA) weather station at the sampling site, including ambient temperature (T), relative humidity (RH), wind speed (WS) and wind direction (WD) were also obtained.

2.3 Chemical analysis

A 0.5 cm^2 ~~piece of quartz~~ punch from each filter was ~~punched and~~ used to determine the concentration of organic carbon (OC) and elemental carbon (EC) ~~content~~ in $PM_{2.5}$. The ~~rest~~remaining portion of ~~the~~each filter was extracted by ultrasonication with 22 mL Milli-Q water (18.2 MΩcm) for 40 minutes~~ and filtered~~, followed by filtration through a 0.45μm PTFE membrane filter (PALL Life Sciences, Ann Arbor, MI, USA). A suite of advanced instruments were employed to analyze the filtrate to characterize its chemical composition and optical properties, including ~~Ion Chromatography~~a total organic carbon (TOC) analyzer for quantifying carbonaceous content, ion chromatography (IC) ~~for~~to measure water soluble ~~ion speciation, Ultraviolet-Visible~~ions, ultraviolet-visible (UV-Vis) spectroscopy ~~for~~to obtain absorbance ~~spectrum~~spectra of water-soluble organic carbon (WSOC~~, Excitation-Emission Matrix~~), excitation-emission matrix (EEM) fluorescence spectroscopy ~~for assessing~~ to assess the fluorescence characteristics of dissolved organic matter, ~~Total Organic Carbon (TOC) analyzer for quantifying carbonaceous content,~~ and offline analysis using a ~~High-Resolution Time-of-Flight Aerosol Mass Spectrometer (~~high-resolution time-of-flight aerosol mass spectrometer (HR-ToF-AMS) ~~for~~ to investigate the detailed

~~aerosol composition~~chemical composition of OA. Our measurement strategy aimed to capture the chemical composition of $PM_{2.5}$ as comprehensively as possible. The chemical species were broadly categorized into inorganic and organic constituents. Inorganic components were quantified using IC, while organic species were determined based on organic carbon measurements. Additionally, the optical properties of organic species were characterized using UV-Vis and EEM spectroscopy. Detailed descriptions of each measurement are provided below.

2.3.1 ~~OC&EC~~Measurements of carbonaceous materials

The OC/EC analysis was ~~performed~~conducted using a ~~Thermal~~thermal/optical ~~Carbon Analyzer~~carbon analyzer (DRI Model 2001; Desert Research Institute, Las Vegas, NV, USA) with the IMPROVE-A ~~method~~protocol (Chow et al., 2007). The 0.5 cm^2 quartz filter was loaded into the instrument, and then ~~incrementally~~sequentially heated ~~to 120~~in a non-oxidizing helium atmosphere to 140℃ (OC1), ~~250~~280℃ (OC2), ~~450~~480℃ (OC3) and ~~550~~580℃ (OC4~~), respectively,~~) to ~~vaporize~~volatilize OC fraction. Then ~~it~~the sample was heated ~~at 550~~in an oxidizing atmosphere (98% He/2% O_2) to 580℃ (EC1), ~~700~~740℃ (EC2), ~~800~~840℃ (EC3) ~~with oxidizing gas and 98% He/2% O_2 as carrier gas to vaporize EC.~~to evolve EC. At each designated temperature ~~stage,~~step, evolved carbon ~~is~~was oxidized to CO_2 and then reduced to CH_4 by H_2 catalyzed by MnO_2. Ultimately, the hydrogen flame ionization detector ~~is~~was utilized to quantify the concentration of the resulting CH_4. In some samples, EC concentrations were below the ~~EC concentration was lower than the minimum~~ detection limit~~,~~ and ~~the EC content was not detected~~thus reported as non-detectable.

WSOC was quantified by a total organic carbon analyzer (Elementar vario TOC cube, Hanau, Germany) with the method of total inorganic carbon (TIC) subtracted from total carbon (TC) ($TOC = TC - TIC$). In this method, TC was determined by converting the carbonaceous matter into CO_2 at 850 °C using platinum as the catalyst and oxygen as the carrier gas. TIC was transformed into CO_2 gas by acidification with 4% phosphoric acid. The resulting CO_2 was quantified using a non-dispersive infrared (NDIR) gas analyzer integrated within the instrument. Prior to the measurement, the instrument was calibrated with standard solutions of potassium hydrogen phthalate and sodium carbonate (Zhang et al., 2017b).

2.3.2 Ion chromatography analysis

Eight water-soluble ionic species (WSIs) (Na^+, NH_4^+, K^+, Ca^{2+}, Mg^{2+}, Cl^-, NO_3^-, SO_4^{2-}) were ~~determined~~quantified using two 881 ~~ion chromatography~~IC systems (Metrohm, Herisau, Switzerland). The ~~cation~~anion system ~~is~~was facilitated by a Metrosep A Supp 5-250/4.0 column ~~(Metrohm). The~~ , with an eluent ~~composition consists~~consisting of 3.2 mM Na_2CO_3 and 1.0 mM $NaHCO_3$, delivered at a flow rate of 0.7 mL min^{-1}. The ~~anionic chromatographic~~cation system ~~is~~was facilitated by a Metrosep C4-250/2.0 column~~. The mobile phase comprises~~ with an eluent of 1.7 mM nitric acid and 0.7 mM dipicolinic acid (DPA), ~~administered~~operated at a flow rate of 0.3 mL min^{-1}. To ensure optimal separation efficiency, ~~the two~~both columns ~~temperature are~~ were maintained at 30~~°C, respectively.~~°C. Prior to ~~sample~~ analysis, the instrument ~~undergoes~~was calibrated using a ~~rigorous~~series of standard solutions to generate accurate calibration ~~process. The IC measurements are~~curves. Sample concentrations were determined by ~~analyzing~~comparing the retention ~~time of the peaks~~times and ~~the~~ integrated peak areas~~. These analytical parameters are then correlated with the calibration curve, which has been previously established using a series of standard solutions, to ensure accurate quantification of the analytes~~ of measured ions with those of the standards (Xu et al., 2015).

2.3.3 UV-vis

~~The ultraviolet visible (UV-Vis)~~ absorption ~~spectrum~~measurements and analysis

The ultraviolet-visible (UV-Vis) absorption spectra of the samples ~~was~~were measured over ~~a~~the wavelength range of 200~~ nm~~–900 nm~~, with~~ at a resolution of 1nm~~,~~ using a dual-beam UV spectrometer (UV-2700, Shimadzu, Kyoto, Japan). ~~Samples~~The water extracts were ~~positioned~~placed in ~~a quartz cuvette with an optical~~ 1cm path length ~~of 1cm~~quartz cuvettes and scanned at a rate of 5 nm s^{-1}, utilizing a dual light source system comprising deuterium and tungsten lamps. ~~To correct baseline, the spectra of all samples were subtracted from the mean absorption value of the corresponding sample at 695 nm – 705 nm~~Baseline correction was performed by

subtracting the mean absorbance value in the 695–705 nm from the entire spectrum for each sample, assuming negligible light absorption by BrC at this wavelength interval.

The absorption coefficient (Abs_λ) is calculated by Eq. (1) (Murphy et al., 2010).

$$Abs_\lambda = (A_\lambda - A_{700})\frac{V_l}{V_a \cdot l} \cdot \ln(10) \quad (1)$$

where A_λ (M m^{-1}) is the absorption coefficient at a specific wavelength; A_{700} is the mean absorption value at 695 nm–705 nm; l is the light distance of the samples during the determination; V_l is the volume of water used in extraction; V_a is the volume of gas that passes through the quartz filter. In general, the absorption coefficient at wavelength 365 nm is used to refer to the absorption of brown carbon. The wavelength dependence of brown carbon absorption can be expressed by Eq. (2).

$$Abs_\lambda = K \cdot \lambda^{-AAE} \quad (2)$$

where K is a constant related to aerosol mass concentration; AAE is the absorption Ångström exponent of particulate matter, which is obtained by linear fitting the natural logarithm of the wavelength (300 nm–400 nm) to the natural logarithm of the corresponding Abs_λ. To calculate the light absorption intensity of unit mass WSOC at a certain wavelength, the mass absorption cross section (MAE) is calculated by Eq. (3).

$$MAE = \frac{Abs_\lambda}{C_{wsoc}} \quad (3)$$

where C_{wsoc} (μgC m^{-3}) is the concentration of water-soluble organic carbon in the atmosphere.

2.3.4 EEM fluorescence spectra analysis

The three-dimensional excitation-emission matrix (3D-EEM) fluorescence spectra of the samples was ~~scanned~~measured by an F-7100 fluorescence spectrometer (Hitachi High-Technologies, Tokyo, Japan~~), using~~) equipped with 700-V xenon arc lamp as the excitation source. During the scanning process, the excitation (Ex) wavelengths ranged from 200 to 450 nm with ~~intervals of~~a 5 nm interval, while the emission (Em) wavelengths spanned from 250 to 600 nm with ~~intervals of~~a 1 nm interval. In this study, Milli-Q water (18.2 MΩ cm^{-1}) was used as ~~a blank value for~~the reference~~. Blank~~ blank. To minimize instrumental interference, the blank reference was subtracted from ~~the~~each sample

EEM ~~fluorescence spectra of the samples to eliminate the impacts of instrument to mitigate the instrumental effects. Once the~~. The corrected EEMs were ~~corrected, they were~~then converted to Raman units (R.U~~.), after which the EEMs were~~.) and subjected to ~~modeling~~further analysis (Murphy et al., 2013). Parallel factor analysis (PARAFAC), ~~which is~~ a three-way decomposition method, ~~divides organic matter into different~~was applied to identify individual fluorescent components based on ~~the~~their spectral similarity ~~of fluorescence characteristics~~. In addition to knowing the relative contribution of each component to the total fluorescence of organic matter, this method also provides information on the biochemical composition, origin, and ~~biogeochemical action of the samples~~transformation processes of organic matter (Fellman et al., 2010). The PARAFAC modeling was performed using DOMfluor and drEEM toolboxes installed on Matlab R2019a in this study. The ~~entire process encompassed several stages:~~workflow included data preprocessing and preliminary analysis, ~~followed by~~ model construction and validation, and culminating in the presentation of the final results (Stedmon and Bro, 2008).

~~In this study~~To further characterize the fluorescence characteristics, humification index (HIX) and biological index (BIX) were ~~used to analyze fluorescence spectral characteristics~~calculated following established methods (Yang et al., 2020; Zhai et al., 2022). ~~Notably, the HIX values exhibit disparities due to~~Given the ~~distinct origins~~differences in origin and transformation ~~pathways of aerosol~~processes between atmospheric and aquatic samples~~. Therefore~~, the emission wavelength ~~selected~~ranges used for HIX calculation ~~was~~were adjusted ~~(~~from the ~~commonly used~~conventional 300-345nm ~~to 325-365nm,~~ and 435-480nm to 325-365nm and 410-450nm~~),~~ respectively (Wen et al., 2021; Wu et al., 2021). The ~~above two optical indices can be~~HIX and BIX were calculated ~~from~~according Eq. (4) and Eq. (5), respectively (Zsolnay et al., 1999).

$$HIX = \frac{\sum SFI(410nm \le \lambda_{Em} \le 450nm)}{\sum SFI(325nm \le \lambda_{Em} \le 365nm)} (\lambda_{Ex} = 225nm) \quad (4)$$

$$BIX = \frac{SFI(\lambda_{Em} = 380nm)}{SFI(\lambda_{Em} = 430nm)} (\lambda_{Ex} = 310nm) \quad (5)$$

where λ_{Em} is the emission wavelength; λ_{Ex} is the excitation wavelength.

2.3.5 ~~WSOC~~

~~Water-soluble organic carbon (WSOC) was measured by a total organic carbon analyzer (Elementar vario TOC cube, Hanau, Germany). The measurement was conducted by applying the total carbon (TC) and total inorganic carbon (TIC) method ($TOC = TC - TIC$). With oxygen as the carrier gas and platinum as the catalyst, inorganic carbon was transformed into CO_2 gas following acidification with 4% phosphoric acid. The concentration of CO_2 was determined using a non-infrared gas detector integrated within the instrument. Prior to the measurement, the total organic carbon (TOC) analyzer was calibrated with standard solutions of potassium hydrogen phthalate and sodium carbonate to ensure accurate quantification (Zhang et al., 2017).~~

~~2.3.6~~ HR-ToF-AMS off-line ~~analysis~~measurement and PMF source decomposition

The High-Resolution Time-of-flight Aerosol Mass Spectrometer (HR-ToF-AMS, Aerodyne Inc., Billerica, MA, USA) ~~can~~was employed to obtain the information of chemical composition and ~~particle size~~elemental ratios of ~~non-refractory aerosol in real Time. HR-ToF-AMS mainly measures particles in the particle size range of 40–1000 nm. The instrument can not only observe aerosols online, but also analyze atomized aerosol extracts offline~~OA (Xu et al., 2015). Using argon as carrier gas, the samples were aerosolized ~~and collected. The aerosol particles enter~~ into the ~~HR-ToF-AMS through~~instrument concentrated by an aerodynamic lens~~, pass through a vacuum chamber and reach the hot surface at 600°C where they are~~ and vaporized ~~instantly. Finally, it is bombarded~~ at 600°C. The resulting vapors were ionized with a 70 eV electron source and ~~ionized into positively charged ion fragments, which enter the~~analyzed by time-of-flight mass ~~spectrometer for the detection of chemical components~~spectrometry. According to the different shapes of ion flight paths in the mass spectrum, HR-ToF-AMS has two operating modes, namely V-mode and W-mode. ~~By comparing the~~ V-mode data ~~of W-mode and V-mode, we choose the data of V-mode~~were selected for ~~the~~ subsequent analysis~~.~~ due to better performance in this study. The data is processed using standard ToF-AMS data analysis ~~software (Igor Pro 6.37). The software includes standard data processing~~ toolkits SQUIRREL (v1.56) and PIKA (v1.15c~~).~~) within Igor Pro 6.37. The processed matrix data

were employed to investigate the sources of WSOA by positive matrix factorization (PMF). PMF source analysis ~~is usually~~was processed using the standard PMF evaluation tool (PET v2.03) developed based on ~~Igor Pro software and~~ the PMF2.exe algorithm (Ulbrich et al., 2009). Based on the Improved Ambient (I-A) method, relevant ~~information of elemental analysis~~ratios including oxygen-to-carbon ~~ratio~~ (O/C), hydrogen-to-carbon ~~ratio~~ (H/C), nitrogen-to-carbon ~~ratio~~ (N/C~~)~~), and ~~ratio of~~the organic matter to organic carbon (OM/OC) ~~can be~~ratio were obtained. The mass concentration of OM ~~can be calculated using~~was estimated according to Eq. (6).

$$OM = OC \times (OM/OC) \quad (6)$$

where OC is the mass concentration of OC measured by Thermal/optical Carbon Analyzer, OM/OC is the ratio obtained from the ~~above~~HR-ToF-AMS.

~~2.3.7 Backward Trajectory Model~~

2.3.6 Source identification using backward trajectory model

To ~~understand~~investigate the possible ~~source~~sources and transport pathways of ~~the~~ air ~~mass~~masses during the sampling, the HYbrid Single-Particle Lagrangian Integrated Trajectory (HYSPLIT) model developed by the National Ocean and Atmospheric Administration (NOAA) and the Australian Bureau of Meteorology was used to calculate ~~and analyze the~~ backward ~~transport trajectory of the~~ air mass trajectories (Stein et al., 2015). ~~The meteorological~~Meteorological data used in this study ~~are~~were Global Data Assimilation System (GDAS) from the National Centers for Environmental Prediction (NECP), with 1°× 1° horizontal resolution. In the calculation, the arrival height ~~of observation station is~~ was set as 500 meters above the ground ~~from~~at the sampling site. Thereafter, hourly backward trajectories were ~~performed~~calculated for a duration of 72 hours to trace the air mass movements~~. Furthermore, the average backward trajectory cluster of the air mass~~ during the whole sampling period ~~was determined by~~. To identify representative transport pathway, cluster analysis was performed based on assessing the spatial ~~distribution~~ similarities across all ~~calculated~~ trajectories.

~~The~~ To further assess potential source regions, the concentration-weighted trajectory (CWT) ~~was~~

~~used to analyze the source of pollution to the sampling site~~method was applied. The CWT is a mixed-trajectory receptor model that combines meteorological trajectory nodes (residence time) and pollutant concentrations to trace their contributions to the pollution of a recipient site. ~~After the~~The study area was ~~firstly~~first gridded with a resolution of 0.25° × 0.25°, the CWT value of Grid (i, j) was calculated as follows:

$$CWT_{ij} = \frac{\sum_{l=1}^{M} C_l t_{ijl}}{\sum_{l=1}^{M} t_{ijl}} W_{ij} \quad (7)$$

$$W_{ij} = \begin{cases} 1.0\left(n_{ij} > 4n_{ave}\right); \\ 0.7\left(4n_{ave} > n_{ij} > n_{ave}\right); \\ 0.42\left(n_{ave} > n_{ij} > 0.5n_{ave}\right); \\ 0.05\left(n_{ij} < n_{ave}\right) \end{cases} \quad (8)$$

where CWT_{ij} is the average weighted concentration in the cell ij; M is the total number of trajectories; C_l is the pollutant concentration when the trajectory l through the grid ij; t_{ijl} is the time that the trajectory l stayed in the grid ij; W_{ij} is the weight factor used to reduce the uncertainty of the calculation; n_{ij} is the number of trajectory endpoints of grid ij, and n_{ave} is the average number of trajectory endpoints. In this way, the CWT model is able to reveal regions that contribute significantly to the concentration of pollutants at the receptor site.

3 Results and discussion

During the sampling period, the meteorological conditions exhibited notable seasonal variations ~~(Figure 2a).~~ The average air temperature (±1σ) was 1.8 ± 8.3℃, with a daily maximum of 13.8 ℃ recorded on July 27, 2019, and a minimum of –15.8℃ on December 26, 2019. Relative humidity (RH) ranged from 10% to 99%, with an average of 57 ± 28.1%. Seasonally, the average air temperatures were –2.7 ± 5.1℃ in spring, 9.1 ± 3.5℃ in summer, –1.6 ± 6.1℃ in fall, and –10.0 ± 3.9℃ in winter. Similarly, the average RH values were 47.0 ± 29.4% in spring, 88.3 ± 12.4% in summer, 68.3 ± 18.5% in fall, and 32.0 ± 16.1% in winter. (Figure 2b). Wind patterns were predominantly from the west during winter, with a ~~step~~visible increase from the east during spring~~,~~ ~~reaching~~. This easterly wind reached the ~~predominance from the east~~maximum in summer. ~~Fall represented~~, reflecting a ~~transitional period~~transition from the winter westerlies to summer monsoon systems (Figure 2a ~~and 2b~~). Precipitation ~~occurred primarily~~exhibited strong seasonality in ~~summer~~

~~(~~both quantity and frequency. Summer contributed 66.9~~%), followed by fall (17.2%) and spring (15.0%), with winter experiencing~~% of the ~~least~~annual precipitation ~~(0.9%).~~ but accounted for 44.0% of the precipitation days, indicating concentrated heavy rainfall. In contrast, autumn contributed 17.2% of the total precipitation but 28.4% days, characteristic of prolonged light rainfalls.

3.1 Chemical ~~speciation~~composition of $PM_{2.5}$

The total mass concentration of all species (WSIs + OM + EC) ranged from 2.0 μg m^{-3} to 41.8 μg m^{-3} during the study period, with a mean of 10.3 ± 7.4 μg m^{-3} (Figure 2d). OM was the major contributor to aerosol mass concentration during the whole period with an average ~~contribution~~value of 37.7%, followed by sulfate (21.3%), nitrate (12.1%), EC (1.1%), and other inorganic ions, which together accounted for ~~29.0~~27.8% (including 7.5% Na^+, 7.6% NH_4^+, 1.~~8~~7% K^+, 6.~~7~~6% Ca^{2+}, 0.8% Mg^{2+}, and 3.6% Cl^-~~) (Figure 2c).~~). The mass concentrations were higher during spring (14.0 μg m^{-3}) and winter (12.5 μg m^{-3}), while relatively lower values were observed in summer (7.1 μg m^{-3}) and fall (8.0 μg m^{-3}) (Figure 2c). These seasonal patterns were driven by increased transport of polluted air masses from the east in winter and prevalent mineral dust storms in spring. The natural mineral dust reached its peak in spring (~~7.5%~~1.05 μg m^{-3} of Ca^{2+}) and its minimum in summer (~~4.1%~~0.29 μg m^{-3} of Ca^{2+}~~).~~) (Figure 2c). The anthropogenic ~~pollution markers~~species (SO_4^{2-} + NO_3^-) accounted for 33.2% of the mass in spring and 32.8% in winter. Among the secondary inorganic ions (sulfate, nitrate, and ammonium), sulfate was the most abundant, especially in summer, when its proportion reached 28.6%, similar to observations ~~made by our group~~conducted in July 2017 (Zhang et al., 2019). Sulfate formation during summer was mainly attributed to strong solar radiation, high humidity, and the heterogeneous reaction of SO_2 (Luo et al., 2022). In contrast, nitrate showed its minimum in summer (10.9%) and its maximum in winter (15.5%), which was mainly controlled by temperature-dependent partitioning. The average nitrate concentrations was 1.4 μg m^{-3} with 2.0 μg m^{-3} in spring, 0.8 μg m^{-3} in summer, 0.9 μg m^{-3} in fall, 1.9 μg m^{-3} in winter in this study, which are comparable to measurements at WLG in July 2017 (0.7 μg m^{-3}) (Zhang et al., 2019) and at sites around the region, such as Qinghai Lake in the summer of 2010 (0.8 ± 0.5 μg m^{-3}) (Li et al., 2013) and Menyuan in autumn 2013 (1.7 μg m^{-3}) (Han et al., 2020). However, these concentrations are significantly higher than those recorded in the western Qilian Mountains, such

as the summer 2012 observation at the Qilian Shan Station of Glaciology and Ecologic Environment (QSS) (0.6 μg m^{-3}) (Xu et al., 2015).

Ion balance, represented by the ratio of cation equivalent concentration (CE, neq m^{-3}) to anion equivalent concentration (AE, neq m^{-3}), was used to assess potential missing ions or the acid-base properties of aerosols (Xu et al., 2014; Xu et al., 2015). The CE/AE ratio calculated in this study was 1.43 (Figure 3a), suggesting the potential presence of acidic aerosols, although carbonate and bicarbonate ions were not measured in the IC analysis. Assuming $2*[HCO_3^-] = [Ca^{2+}]$, the estimated CE/AE is still 1.35. In addition, the ratio of $[SO_4^{2-} + NO_3^-]$ to $[NH_4^+]$ was 1.94, indicating that there was an excess of sulfuric and nitric acids. The acidic property in the aerosol of our study can be further supported by a significant number of organic acids, such as oxalic acid (Figure 3b). Oxalic acid is a product of atmospheric photochemical aging and is closely associated with sulfate and aerosol liquid water (Yang et al., 2009; Huang et al., 2019; Xu et al., 2020b; Boreddy et al., 2023). A ~~moderate~~significant correlation was found between oxalic acid peak area and sulfate during summer (~~R^2=~~Pearson's r = 0.~~4~~61, $P < 0.05$) (Figure 3c).

Air mass backward trajectory analysis ~~enables the initial tracing of potential sources and transport pathways of atmospheric aerosols throughout the observation period (Figure 4). Air~~suggests that air mass origination varied from east to west seasonally, with the east mainly occurred during the summer transported with a shorter distance and the west during winter with a longer distance~~.~~ (Figure 4). Specifically, the fraction of the air mass from the east was up to 50.5% in spring and 66.0% in summer and the mostly potential source areas for pollutants were predominantly associated with these air masses (Figure 5). The less important source areas are also observed from the north and west, especially during the fall, when the climatic systems of summer monsoon and the westerlies interacted. In these directions, widely distributed mineral dust source areas and sparse urban cities are located. Overall, anthropogenic emissions located in the east of WLG emerge as the most significant ~~sources~~source regions to the WLG.

3.2 Optical properties of WS-BrC

The average absorption coefficient ~~(Abs_{365})~~ of WS-BrC at 365nm (Abs_{365}) was 1.15 ± 0.97 Mm^{-1}. The Abs_{365} was much higher in spring and winter than in summer and fall (1.55 ± 1.30 Mm^{-1} in winter and 1.45 ± 0.54 Mm^{-1} in spring vs. 0.88 ± 0.70 Mm^{-1} in fall and 0.36 ± 0.21 Mm^{-1} in summer), which is consistent with the distribution of OM mass concentration. The average absorption efficiency of WS-BrC at unit WSOC content (MAE) during the summer at 365nm (MAE_{365}, 0.40 ± 0.24 m^2g^{-1}) is significantly lower than that of the other three seasons (0.92 ± 0.54 m^2g^{-1} in spring, 0.81 ± 0.46 m^2g^{-1} in fall and 0.97 ± 0.49 m^2g^{-1} in winter) (Figure 6a~~), suggesting highly photobleaching of BrC.~~). A low MAE_{365} value may result from either a reduced abundance of light-absorbing chromophores or photobleaching effects. However, we propose that photobleaching plays a predominant role, based on the observed negative correlation between MAE_{365} and the oxidation state of OA (see section 3.5). MAE_{365} in summer is comparable to that at WLG (0.48 m^2g^{-1}) in July 2017 (Xu et al., 2020a), Nam Co (0.38 m^2g^{-1}) from May 13 to July 1, 2015 (Zhang et al., ~~2017~~2017a) and the regional background points of North China Plain (0.38 m^2g^{-1}) in summer of 2017 (Luo et al., 2020). But the MAE_{365} in spring of this study (0.92 ± 0.54 m^2g^{-1}) is at a high level over the TP and even higher than the Qomolangma Station (QOMS) (0.81 m^2g^{-1}) which is frequently impacted by biomass burning emission (Xu et al., 2020a).

AAE of light absorption spectrum is an important optical parameter to check the containing of BrC in aerosols. In the 300–400 nm range, a high AAE value indicates significant aerosol absorption of shortwave ultraviolet light, with a relatively higher contribution from BrC. This phenomenon is typically observed in cases from biomass burning emission, secondary organic aerosols (SOA), and anthropogenic pollutant emissions (Siemens et al., 2022; Tao et al., 2024). The AAE (300 ~~nm~~ – 400 nm) in this study ranges from 3.06 to 8.42, with an annual average of 5.42 ± 1.26 and peaking in summer ~~at (~~6.21 ± 1.50~~,~~), followed by 5.48 ± 0.96 in winter, 5.19 ± 1.00 in fall, and 5.14 ± 1.46 in spring (Figure 6a). The average annual AAE is comparable with the observation at Lulang (5.39 ± 1.22~~)~~, 330 – 400 nm), in the southeastern part of the TP, during August 2014 to August 2015 ~~at the southeastern TP~~ (Li et al., ~~2016~~2016b)~~. The summertime AAE is similar to those at other stations in TP, such as Nam Co (5.91 ± 2.14) from May 13 to July 1, 2015 (Zhang et al., 2017) and WLG (5.96)~~

from July 2017, but lower than those observed at QOMS (6.83) from April 12 to May 12, 2016 (Xu et al., 2020a). and Lhasa (5.38, 330 – 400 nm) during May 2013 to March 2014, a typical urban area on the TP (Li et al., 2016a). The summertime AAE is also similar to those at other stations on the TP, such as Nam Co (5.91 ± 2.14, 300 – 400 nm) from May 13 to July 1, 2015 (Zhang et al., 2017a) and WLG (5.96, 300 – 400 nm) from July 2017 (Xu et al., 2020a). The AAE value in winter is closed to that observed in the eastern Himalayas (5.5, 300 – 450 nm) during the 2019-2020 winter (Arun et al., 2024).

Figure 6b illustrates the comparison of optical properties of WSOA in the map space of AAE (300 nm – 400 nm) versus the logarithm of MAE_{365} proposed by Saleh (2020). This map can be categorized into four classes as MAE_{365} increase and $AAE_{300\text{-}400}$ decreases, which are associated with increased molecular sizes, decreased volatility, reduced solubility in water/organic solvents, and lower susceptibility to photobleaching. All our samples collected fall within the weakly absorbing BrC (W-BrC) category. This result is consistent with previous findings from QOMS and WLG reported by our group (Xu et al., 2022). In addition, the samples collected from other stations across the TP, including Nam Co station during summer (Zhang et al., 2017), Lulang station during summer and winter (Wu et al., 2020), and Xining urban station during winter (Zhong et al., 2023), were also distributed in the W-BrC category. These results suggest that the samples at WLG during four seasons are aged BrC. Note that lower AAE and higher MAE_{365} observed in spring were closer to moderately absorptive brown carbon (M-BrC) suggesting less oxidization.In our dataset, the majority of data points fall within the region corresponding to weakly absorbing brown carbon (W-BrC). This suggests that the OA at WLG were overall aged BrC, which is consistent with observations from other remote sites on the TP (Zhang et al., 2017a; Wu et al., 2020; Xu et al., 2022; Zhong et al., 2023). A limited number of data points, primarily from the spring, deviate from this pattern and fall closer to the region associated with moderately absorbing BrC (M-BrC). These outliers are likely influenced by episodic inputs of anthropogenic aerosols from surrounding populated areas.

3.3 Fluorescent components and fluorescence indices

PARAFAC analysis ~~identify~~identified four components (C1-C4) in this study (Figure 7a). The chemical properties of each component ~~are~~were determined based on the comparison with previous studies (Chen et al., 2016a; Chen et al., 2016b; Chen et al., 2020; Yu et al., 2023; Zhong et al., 2023). C1 ~~is~~was determined as ~~high-oxidation humus~~a highly oxidized humic-like component (HULIS-1) with ~~the peaks of~~ Ex ~~and~~ /Em maxima at 240 ~~nm and~~ /413 nm ~~(Ex/Em = 240/413 nm)~~ (Tang et al., 2024). C2 (Ex/Em = 225/375 nm) ~~is~~was classified as ~~low-oxidation humus~~a less oxidized humic-like component (HULIS-2), ~~which is generally~~typically associated with combustion-related source (Li et al., 2022; Afsana et al., 2023). Both C3 (Ex/Em = 280 /358 nm) and C4 (Ex/Em = 225(270)/297 nm) were classified as protein-like organic matter (PLOM) (Wang et al., 2024). C3 ~~is~~was probably a fossil fuel-related substance (Wu et al., 2019) ~~and~~, while C4 ~~has~~had a main peak and a secondary peak similar to the ~~characteristics~~characteristic of tyrosine-like chromophore (Chen et al., 2016b; Chen et al., 2021b). HULIS compounds (C1 and C2) dominated the annual average contribution by 57.9%, of which C1 accounted for 22.9% and C2 accounted for 35.0%. PLOM contributed an average of 42.1%, with C4 accounting for 27.0% and C3 being 15.1% (Figure 7b). C1 ~~presents a~~presented weak seasonal variation peaking in summer (23.54%) corresponding to the highest intensity of photochemical oxidation ~~and contributing the least in spring (21.8%).~~. The average relative contribution of C2 was 37.0%, 35.0%, 33.6% and 34.4% in spring, summer, fall and winter, respectively. ~~The average~~ In contrast, C3 showed higher relative ~~contribution of C3~~ contributions in spring (17.8%) and winter (17.0%) ~~is higher~~ than ~~that~~ in summer (12.6%) and fall (13.1%), which may be related to frequent coal-burning emissions during heating period. ~~In contrast~~Conversely, the contribution of C4 ~~is~~was significantly more pronounced during summer (28.9%) and fall (30.5%) than that in spring (23.4%) and winter (25.1%), ~~Corresponding~~corresponding to enhanced activities in agriculture emissions and ~~ecology~~ecological activities (Zheng et al., 2016; Zhang et al., 2020).

The fluorescence indices BIX and HIX serve as complementary tools for characterizing fluorescent OM. BIX is particularly used to assess the biological freshness of OM, whereas HIX reflects the degree of humification and chemical aging (Lee et al., 2013). By integrating these two indices, a

more comprehensive understanding of the properties of OM can be achieved. An elevated degree of aging ~~in WSOA~~ is associated with ~~an~~ increased HIX ~~value~~values (Fan et al., 2020; Wu et al., 2021; Ma et al., 2022) and ~~a~~ decreased BIX ~~value~~values (Wen et al., 2021). In this study, the annual average HIX and BIX values ~~are~~were 1.11 ± 0.18 and 1.29 ± 0.14, respectively, with seasonal variations of 1.04 ± 0.16 and 1.39 ± 0.24 in spring, 1.24 ± 0.11 and 1.26 ± 0.13 in summer, 1.13 ± 0.20 and 1.23 ± 0.09 in fall, and 1.02 ± 0.17 and 1.29 ± 0.09 in winter. The spring samples ~~exhibit~~exhibited the greatest variability, indicating their ~~fresher~~relatively fresh properties (Figure 8b). ~~Summer season is~~In contrast, summer was characterized by the highest HIX ~~and the low BIX~~, suggesting a high degree of aging and oxidation ~~of WS-BrC. These values are positioned in the upper left corner of HIX versus BIX space~~. The HIX of the autumn samples were at an intermediate level, while winter samples had the lowest HIX and moderate BIX values, indicating the lower degree of oxidation (Figure 8a). ~~Comparing~~Compared with ~~the results of~~ previous ~~study~~studies, the fluorescence properties of aerosols in this study are more consistent with those in the northwestern China ~~(Figure 8) (Chen et al., 2021a; Zhang et al., 2021a; Zhong et al., 2023), which is~~, and were less humified than ~~that~~those in the eastern China ~~.~~ (Figure 8) (Chen et al., 2021a; Zhang et al., 2021a; Zhong et al., 2023).

3.4 Chemical components of WSOA and their light absorption

PMF ~~decomposes~~decomposed the WSOA into two factors, i.e., a more oxidized oxygenated OA (MO-OOA) and a less oxidized oxygenated OA (LO-OOA) (Figure 9a). ~~The~~Note that since our PMF analysis was conducted solely on the water-soluble fraction of OA, hydrophobic primary components may not be captured effectively. The mass spectra of these two OOAs in this study ~~are~~were consistent with those of online measurement at Nam Co Station in the TP during the summer (Xu et al., 2018). The average mass contribution of LO-OOA and MO-OOA were 47% and 53% (Figure 9c), respectively. The mass contribution of MO-OOA across the four seasons (spring to winter) was 55.4%, 54.9%, 61.7% and 42.0%, respectively. The time series of LO-OOA correlated well with ~~sulfate~~nitrate (R^2=0.47) during winter and ~~less well~~weak correlation with ~~nitrate~~sulfate (R^2=0.39), while MO-OOA correlated poorly with ~~sulfate and nitrate~~both species (Figure 9b).

The triangle plot of *m/z* 44 (*f*44) versus *m/z* 43 (*f*43) and Van Krevelen diagram of elemental ratios are valuable tools for examining the ambient evolution of OA (Ng et al., 2010; Zhang et al., 2019; Chazeau et al., 2022). *f*44 is associated with highly ~~with~~ oxidized oxygenated OA, while *f*43 corresponds to less oxidized OA. During atmospheric oxidation, OA ~~transited~~generally evolves from a lower to a higher oxidation state, characterized by an increase in *f*44 and a decrease in *f*43, moving from the base to the apex of the triangular plot (Flores et al., 2014). ~~Most~~In this study, most data points ~~in our study locate~~were located in the upper ~~section~~region of this triangular suggesting an overall high degree of oxidation across the dataset (Figure 9e~~) with data points during~~). Samples in winter were at ~~a~~the lower position and ~~data points~~samples during summer ~~shifting towards~~shifted toward the higher position, presenting a distinct oxidation degree at different seasons. ~~–~~The Van Krevelen plot provides further ~~elucidates~~insights into the chemical ~~transformations~~evolution of OA during atmospheric aging (Heald et al., 2010; Xu et al., 2018). The ~~transition~~ slope ~~from low to high oxygen states typically ranges from −1 to −0.5 (Ng et al., 2011). In our data,~~of the linear regression in the diagram reflects the predominant oxidation pathways. A slope ~~of all data points~~ between –1 to –0.5 is typically associated with functionalization processes such as the formation of carboxylic acids or alcohol/peroxide groups (Ng et al., 2011). In our dataset, the overall slope was –0.62 (Figure 9f), indicating mixed contributions from both carboxylic acid and alcohol/peroxide formation pathways. This slope was higher than ~~winter's −0.89 at~~the value previously reposted for winter in Xining (–0.89) and ~~summer's~~ summer at NamCo (–0.76~~ at NamCo~~) (Xu et al., 2018; Zhong et al., 2023). Seasonal slopes ~~vary~~varied slightly, with spring and summer both at –0.58, fall at –0.60, and winter at –0.66, indicating the different OA oxidation pathways ~~during each season~~across seasons.

The light absorption characteristics of different WSOA factors, were evaluated by a multiple linear regression (MLR) model, which was applied to ~~assign the WSOA factors~~apportion their contributions to the light absorption at 365 nm (Abs_{365}) (Zhang et al., 2021b; Jiang et al., 2023). The MLR method can be expressed as Eq. (9).

$$Abs_{\lambda} = f_1 \times C_{MO-OOA} + f_2 \times C_{LO-OOA} \quad (9)$$

where f_n is the corresponding fitting coefficients, which can also represent the mass absorption cross section (MAC) values of different organic components; C_{MO-OOA} and C_{LO-OOA} (μg m^{-3})

are the mass concentration of the organic components; $f \times C$ is the absorption value of the organic component. The estimated MAC_{365} ~~of the two factors are~~were 0.41 m^2g^{-1} ~~(~~for MO-OOA~~)~~ and 0.45 m^2g^{-1} ~~(~~for LO-OOA~~)~~ (Figure 6a). The MAC_{365} value of LO-OOA ~~is~~was slightly higher than that of MO-OOA, which ~~is~~was related to the relatively weak photobleaching of LO-OOA. Compared to previous studies, $MAC_{365,\ MO\text{-}OOA}$ in this study ~~is~~was lower than $MAC_{370,\ MO\text{-}OOA}$ (0.60 m^2g^{-1}) reported at the QOMS (Zhang et al., 2021b). $MAC_{365,\ LO\text{-}OOA}$ ~~is~~was much lower than that observed ~~in~~at urban ~~stations of Northwest~~sites in northwestern China in winter 2019 (1.33 m^2g^{-1}) (Zhong et al., 2023)~~, which may~~. The differences across sites could be attributed to ~~strong photobleaching of OA~~variations in ~~remote areas during atmospheric transport.~~their chemical composition, sources, and also oxidation state.

3.5 Relationship between oxidation state and optical properties of BrC

During the atmospheric aging ~~process~~ of BrC, changes in its optical properties can reflect concurrent alterations in its chemical characteristics (Alang and Aggarwal, 2024). In this study, we investigated the relationship between the MAE_{365} and the elemental ratios of O/C and H/C across different seasons (Figure10). MAE_{365} exhibited a positive correlation with O/C in spring ($r = 0.63$; $P < 0.01$~~),~~ ~~while an~~) and a weak, statistically insignificant ~~negative~~positive correlation ~~was~~in winter. In contrast, negative correlations were observed in summer and ~~autumn~~fall ($r = -0.29$0.29 and $r = -0.09$~~).~~0.09). ~~Conversely, the relationship between~~These seasonal relationships for MAE_{365} and H/C showed an opposite pattern in each season (Figure 10b). These results suggest that the light absorption capacity of BrC was enhanced during the oxidation process in spring and winter due to functionalization or oligomerization resulting in increased chromophore species, while further oxidation in summer and autumn leads to the fragmentation of large molecular weight compounds, ~~resulting~~leading to photobleaching~~, which diminishes~~ and reduction in the light absorption capacity (Jiang et al., 2022).

~~Furthermore,~~In this study, cross-correlation analysis was performed on the chemical components of $PM_{2.5}$ (SO_4^{2-}, NO_3^-, NH_4^+, K^+, Cl^-, LO-OOA, MO-OOA), oxidation degree (O/C and H/C), and the four PARAFAC-derived fluorescent components (C1 – C4). As illustrated in Figure S1, C1, C2, and

C3 exhibited positive correlations with the secondary species (SO_4^{2-}, NO_3^-, NH_4^+, Cl^-, LO-OOA, and MO-OOA). The strongest correlations were observed between C1 and these species, suggesting a secondary source origin for this chromophore. C2 and C3 showed a moderate correlation with these secondary species. In contrast, C4 showed weak or no significant correlations with any of the chemical components, implying that C4 was not directly related to the oxidation processes of OA. As discussed in Section 3.3, C4 was related to agriculture emissions and ecological activities, rather than secondary atmospheric formation. To better show the optical evolution of WS-BrC during the atmospheric oxidation ~~process was explored by integrating~~processing, the relationships of PARAFAC components ~~with~~and the WSOA components ~~in~~ were integrated into EEM plot (Figure 10c). ~~The compounds are categorized based on their correlation analysis among each other: C1 is strongly~~C1 was associated with MO-OOA, whereas C2 and C3 ~~are~~were linked to LO-OOA, and C4 ~~exhibits a~~exhibited weak ~~correlation~~correlations with these two factors. ~~Through this method, the chemical evolution of different components could be cross-validated and provide~~This classification enables cross-validation of chemical and optical properties, providing additional insights ~~in the plot~~into the formation pathways of chromophore components (Chen et al., 2016b; Zhong et al., 2023). ~~Simply~~Overall, the ~~transition of~~chemical transformation from less oxidized to highly oxidized OA through photochemical reactions can be ~~applied~~extended to the process of BrC. Correspondingly, the optical evolution of BrC can serve as evidence of the oxidative state transition. ~~For our dataset, C1 is likely formed through atmospheric oxidation processes similar to the transition from LO-OOA to MO-OOA, whereas C2 and C3 may originated from primary DOM in less oxidized region. C4 is the protein-like compound and has weak connection with OOA species.~~

4 Conclusions

In this study, year-long atmospheric aerosol samples collected at WLG were analyzed~~, focusing on~~ to investigate their chemical composition, optical properties, ~~and~~ sources~~. The main conclusions are as follows:~~

~~OM is~~, and seasonal behaviors. OA was the ~~largest~~dominant component of $PM_{2.5}$ throughout the

year, accounting for an annual average of 37.7% of the total mass, followed by sulfate (21.3%) and nitrate (12.1%). ~~Notably, during~~ OA and nitrate concentrations peaked in winter, while sulfate was enhanced in summer, ~~atmospheric~~reflecting distinct seasonal chemical processes and sources. In particular, the summertime increase in sulfate was attributed to intensified photochemical reactions ~~lead to significant sulfate production.~~under strong solar radiation. The light absorption capacity of WS-BrC ~~varies seasonally, with the~~ was overall weak and exhibited distinct seasonal variation. The highest ~~levels~~MAE_{365} was observed in winter~~,~~ (0.97 ± 0.49 m^2 g^{-1}), followed by spring~~,~~ (0.92 ± 0.54 m^2 g^{-1}), fall~~,~~ (0.81 ± 0.46 m^2 g^{-1}), and summer~~. In~~ (0.40 ± 0.24 m^2 g^{-1}). The lowest MAE_{365} in summer~~, the~~ suggested strong photobleaching of OA which could also be illustrated by higher values of AAE and HIX ~~are elevated, likely due to increased oxidation processing of OA. The sources of~~. Backward trajectory analysis indicated that aerosol transport to WLG ~~are~~ predominantly originated from urbanized regions to the ~~eastern urban areas.~~

northeast and east. Four chromophores ~~are~~were identified based on PARAFAC analysis, with HULIS being the predominant contributors to ~~fluorescence.~~fluorescent OA. PMF analysis on OA revealed two factors ~~of~~ (MO-OOA and LO-OOA~~. On average,~~). While MO-OOA ~~is~~was more ~~dominant in mass concentration; however, its~~abundant, LO-OOA exhibited stronger light absorption ~~capacity is lower than that of LO-OOA.~~. Both factors ~~exhibit reduced~~exhibited weaker light absorption compared to those in urban studies, indicating a high level of photochemical ~~oxidation at WLG.~~

aging at this remote site. Integrating the PARAFAC and PMF results, we observed seasonally distinct relationships between O/C ratio and MAE_{365}, highlighting variations in the chemical processing of BrC across seasons. Overall, this study provides valuable insights ~~and serves as~~into the sources, composition, and transformation of BrC in a ~~foundational~~high-altitude background environment. These findings offer a valuable reference for ~~future research on atmospheric~~understanding aerosol ~~conditions in~~-climate interactions and for improving regional climate assessments over the northeastern ~~Tibetan Plateau. The findings will aid efforts to better understand the background characteristics of aerosols in this region~~TP.

Data availability

The data used in this study can be ~~accessed on request from the corresponding author.~~accessible at National Cryosphere Desert Data Center (https://www.doi.org/10.12072/ncdc.nieer.db6809.2025).

Author contributions

JX designed the research and KL, MZ, and WZ collected samples. KL and JX processed data, plotted the figures, and wrote the manuscript when JX and MZ gave constructive discussion. YA and XQ had an active role in supporting the experimental work. All authors contributed to the discussions of the results and refinement of the manuscript.

Competing interests

The authors declare that they have no conflict of interests.

Acknowledgment

This study was supported by grants from the National Natural Science Foundation of China (42476249 and 42021001~~),~~) and the Fundamental Research Funds for the Central Universities. Thanks for the logistic support and assistance from WLG station.

References

Afsana, S., Zhou, R. C., Miyazaki, Y., Tachibana, E., Deshmukh, D. K., Kawamura, K., and Mochida, M.: Fluorescence of solvent-extractable organics in sub-micrometer forest aerosols in Hokkaido, Japan, Atmos. Environ., 303, https://doi.org/10.1016/j.atmosenv.2023.119710, 2023.

Alang, A. K. and Aggarwal, S. G.: Atmospheric Brown Carbon: Sources, Optical Properties, and Chromophore Composition, Aerosol Air Qual. Res., 24, https://doi.org/10.4209/aaqr.240035, 2024.

Arun, B. S., Gogoi, M. M., Deshmukh, D. K., Hegde, P., Boreddy, S. K. R., Borgohain, A., and Babu, S. S.: Enhanced light absorption by ambient brown carbon aerosols in the eastern Himalayas,

Environ. Sci.: Atmos., 4, 782-801, https://doi.org/10.1039/d4ea00021h, 2024.
Boreddy, S. K. R., Kawamura, K., Gowda, D., Deshmukh, D. K., Narasimhulu, K., and Ramagopal, K.: Sulfate-associated liquid water amplifies the formation of oxalic acid at a semi-arid tropical location over peninsular India during winter, Sci. Total. Environ., 874, https://doi.org/10.1016/j.scitotenv.2023.162365, 2023.
Chazeau, B., El Haddad, I., Canonaco, F., Temime-Roussel, B., D'Anna, B., Gille, G., Mesbah, B., Prevot, A. S. H., and Wortham, H.: Organic aerosol source apportionment by using rolling positive matrix factorization: Application to a Mediterranean coastal city, Atmos. Environ.-X, 14, https://doi.org/10.1016/j.aeaoa.2022.100176, 2022.
Che, H. Z., Wang, Y. Q., and Sun, J. Y.: Aerosol optical properties at Mt. Waliguan Observatory, China, Atmos. Environ., 45, 6004-6009, https://doi.org/10.1016/j.atmosenv.2011.07.050, 2011.
Chelluboyina, G. S., Kapoor, T. S., and Chakrabarty, R. K.: Dark brown carbon from wildfires: a potent snow radiative forcing agent?, NPJ Clim. Atmos. Sci., 7, 200, https://doi.org/10.1038/s41612-024-00738-7, 2024.
Chen, J. ~~S.~~ and Wang, C~~.~~ ~~y~~.: Rising springs along the Silk Road, Geology, 37, 243-246, https://doi.org/10.1130/G25472A.1, 2009.
Chen, Q., Hua, X., and Dyussenova, A.: Evolution of the chromophore aerosols and its driving factors in summertime Xi'an, Northwest China, Chemosphere, 281, https://doi.org/10.1016/j.chemosphere.2021.130838, 2021a.
Chen, Q., Ikemori, F., and Mochida, M.: Light Absorption and Excitation-Emission Fluorescence of Urban Organic Aerosol Components and Their Relationship to Chemical Structure, Environ. Sci. Technol., 50, 10859-10868, https://doi.org/10.1021/acs.est.6b02541, 2016a.
Chen, Q., Mu, Z., Xu, L., Wang, M., Wang, J., Shan, M., Fan, X., Song, J., Wang, Y., Lin, P., and Du, L.: Triplet-state organic matter in atmospheric aerosols: Formation characteristics and potential effects on aerosol aging, Atmos. Environ., 252, https://doi.org/10.1016/j.atmosenv.2021.118343, 2021b.
Chen, Q., Li, J., Hua, X., Jiang, X., Mu, Z., Wang, M., Wang, J., Shan, M., Yang, X., Fan, X., Song, J., Wang, Y., Guan, D., and Du, L.: Identification of species and sources of atmospheric chromophores by fluorescence excitation-emission matrix with parallel factor analysis, Sci. Total. Environ., 718, https://doi.org/10.1016/j.scitotenv.2020.137322, 2020.
Chen, Q., Miyazaki, Y., Kawamura, K., Matsumoto, K., Coburn, S., Volkamer, R., Iwamoto, Y., Kagami, S., Deng, Y., Ogawa, S., Ramasamy, S., Kato, S., Ida, A., Kajii, Y., and Mochida, M.: Characterization of Chromophoric Water-Soluble Organic Matter in Urban, Forest, and Marine Aerosols by HR-ToF-AMS Analysis and Excitation-Emission Matrix Spectroscopy, Environ. Sci. Technol., 50, 10351-10360, https://doi.org/10.1021/acs.est.6b01643, 2016b.
Chen, Z. and Torres, O.: An examination of oxidant amounts on secondary organic aerosol formation and aging, Atmos. Environ., 43, 3579-3585, https://doi.org/10.1016/j.atmosenv.2009.03.058, 2009.
Choudhary, V., Gupta, T., and Zhao, R.: Evolution of Brown Carbon Aerosols during Atmospheric Long-Range Transport in the South Asian Outflow and Himalayan Cryosphere, ACS Earth Space Chem., 6, 2335-2347, https://doi.org/10.1021/acsearthspacechem.2c00047, 2022.
Chow, J. C., Watson, J. G., Chen, L. W. A., Chang, M. C. O., Robinson, N. F., Trimble, D., and Kohl, S.: The IMPROVE-A temperature protocol for thermal/optical carbon analysis: maintaining consistency with a long-term database, J. Air Waste Manage., 57, 1014-1023, https://doi.org/10.3155/1047-3289.57.9.1014, 2007.

Dai, M., Zhu, B., Fang, C., Zhou, S., Lu, W., Zhao, D., Ding, D., Pan, C., and Liao, H.: Long-Term Variation and Source Apportionment of Black Carbon at Mt. Waliguan, China, J. Geophys. Res.-Atmos., 126, https://doi.org/10.1029/2021JD035273, 2021.

Fan, L., Yan, X., Du, Q., Zhang, J., Liu, G., Yang, Y., Miao, Y., and Zhang, G.: On the sources of ambient SOA in $PM_{2.5}$: An integrated analysis over Jinan city of China, Atmos. Pollut. Res., 15, https://doi.org/10.1016/j.apr.2023.102008, 2024.

Fan, X., Cao, T., Yu, X., Wang, Y., Xiao, X., Li, F., Xie, Y., Ji, W., Song, J., and Peng, P. a.: The evolutionary behavior of chromophoric brown carbon during ozone aging of fine particles from biomass burning, Atmos Chem Phys, 20, 4593-4605, https://doi.org/10.5194/acp-20-4593-2020, 2020.

Fellman, J. B., Hood, E., and Spencer, R. G. M.: Fluorescence spectroscopy opens new windows into dissolved organic matter dynamics in freshwater ecosystems: A review, Limnol. Oceanogr., 55, 2452-2462, https://doi.org/10.4319/lo.2010.55.6.2452, 2010.

Flores, J. M., Zhao, D. F., Segev, L., Schlag, P., Kiendler-Scharr, A., Fuchs, H., Watne, A. K., Bluvshtein, N., Mentel, T. F., Hallquist, M., and Rudich, Y.: Evolution of the complex refractive index in the UV spectral region in ageing secondary organic aerosol, Atmos Chem Phys, 14, 5793-5806, https://doi.org/10.5194/acp-14-5793-2014, 2014.

Forster, P., Storelvmo, T., Armour, K., Collins, W., Dufresne, J.-L., Frame, D., Lunt, D., Mauritsen, T., Palmer, M., Watanabe, M., Wild, M., and Zhai, P.: "Short-lived Climate Forcers," in Climate Change 2021 – The Physical Science Basis: Working Group I Contribution to the Sixth Assessment Report of the Intergovernmental Panel on Climate Change, Cambridge University Press, 817–922, https://doi.org/10.1017/9781009157896.008, 2021.

Han, B., Yang, W., Wang, J., Zhao, X., Yin, B., Wang, X., Geng, C., Dou, X., Xu, X., and Bai, Z.: Characterizations and Potential Formation Pathways of Atmospheric Inorganic Ions at a National Background Site in the Northeastern Qinghai-Tibet Plateau During Autumn Season, J. Geophys. Res.-Atmos., 125, https://doi.org/10.1029/2020JD032819, 2020.

Heald, C. L., Kroll, J. H., Jimenez, J. L., Docherty, K. S., DeCarlo, P. F., Aiken, A. C., Chen, Q., Martin, S. T., Farmer, D. K., and Artaxo, P.: A simplified description of the evolution of organic aerosol composition in the atmosphere, Geophys. Res. Lett., 37, https://doi.org/10.1029/2010GL042737, 2010.

Huang, X., Zhang, J., Luo, B., Luo, J., Zhang, W., and Rao, Z.: Characterization of oxalic acid-containing particles in summer and winter seasons in Chengdu, China, Atmos. Environ., 198, 133-141, https://doi.org/10.1016/j.atmosenv.2018.10.050, 2019.

Jiang, W., Ma, L., Niedek, C., Anastasio, C., and Zhang, Q.: Chemical and Light-Absorption Properties of Water-Soluble Organic Aerosols in Northern California and Photooxidant Production by Brown Carbon Components, ACS Earth Space Chem., 7, 1107-1119, https://doi.org/10.1021/acsearthspacechem.3c00022, 2023.

Jiang, X., Liu, D., Li, Q., Tian, P., Wu, Y., Li, S., Hu, K., Ding, S., Bi, K., Li, R., Huang, M., Ding, D., Chen, Q., Kong, S., Li, W., Pang, Y., and He, D.: Connecting the Light Absorption of Atmospheric Organic Aerosols with Oxidation State and Polarity, Environ. Sci. Technol., 56, 12873-12885, https://doi.org/10.1021/acs.est.2c02202, 2022.

Klodt, A. L., Aiona, P. K., MacMillan, A. C., Ji Lee, H., Zhang, X., Helgestad, T., Novak, G. A., Lin, P., Laskin, J., Laskin, A., Bertram, T. H., Cappa, C. D., and Nizkorodov, S. A.: Effect of relative humidity, NOx, and ammonia on the physical properties of naphthalene secondary organic

aerosols, Environ. Sci.: Atmos., 3, 991-1007, https://doi.org/10.1039/d3ea00033h, 2023.
Laskin, A., Laskin, J., and Nizkorodov, S. A.: Chemistry of Atmospheric Brown Carbon, Chem. Rev., 115, 4335-4382, https://doi.org/10.1021/cr5006167, 2015.
Lee, H. J., Laskin, A., Laskin, J., and Nizkorodov, S. A.: Excitation-emission spectra and fluorescence quantum yields for fresh and aged biogenic secondary organic aerosols, Environ. Sci. Technol., 47, 5763-5770, https://doi.org/10.1021/es400644c, 2013.
Lee, W. G., Shin, P., and Wang, C.: The influence of relative humidity on the size of atmospheric aerosol, J. Environ. Sci. Health A, 32, 1085-1097, https://doi.org/10.1080/10934529709376597, 2008.
Li, C., Chen, P., Kang, S., Yan, F., Hu, Z., Qu, B., and Sillanpää, M.: Concentrations and light absorption characteristics of carbonaceous aerosol in PM 2.5 and PM 10 of Lhasa city, the Tibetan Plateau, Atmos. Environ., 127, 340-346, http://dx.doi.org/10.1016/j.atmosenv.2015.12.059, 2016a.
Li, C., Yan, F., Kang, S., Chen, P., Hu, Z., Gao, S., Qu, B., and Sillanpää, M.: Light absorption characteristics of carbonaceous aerosols in two remote stations of the southern fringe of the Tibetan Plateau, China, Atmos. Environ., 143, 79-85, https://doi.org/10.1016/j.atmosenv.2016.08.042, ~~2016~~2016b.
Li, J., Wang, G., Wang, X., Cao, J., Sun, T., Cheng, C., Meng, J., Hu, T., and Liu, S.: Abundance, composition and source of atmospheric $PM_{2.5}$ at a remote site in the Tibetan Plateau, China, Tellus B, 65, http://dx.doi.org/10.3402/tellusb.v65i0.20281, 2013.
Li, X., Fu, P., Tripathee, L., Yan, F., Hu, Z., Yu, F., Chen, Q., Li, J., Chen, Q., Cao, J., and Kang, S.: Molecular compositions, optical properties, and implications of dissolved brown carbon in snow/ice on the Tibetan Plateau glaciers, Environ. Int., 164, https://doi.org/10.1016/j.envint.2022.107276, 2022.
Li, Z., Yuan, R., Feng, Q., Zhang, B., Lv, Y., Li, Y., Wei, W., Chen, W., Ning, T., Gui, J., and Shi, Y.: Climate background, relative rate, and runoff effect of multiphase water transformation in Qilian Mountains, the third pole region, Sci. Total. Environ., 663, 315-328, https://doi.org/10.1016/j.scitotenv.2019.01.339, 2019.
Liu, S., Sun, W., Shen, Y., and Li, G.: Glacier changes since the Little Ice Age maximum in the western Qilian Shan, northwest China, and consequences of glacier runoff for water supply, J. Glaciol., 49, 117-124, https://doi.org/10.3189/172756503781830926, 2017.
Liu, Y., Hua, S., Jia, R., and Huang, J.: Effect of Aerosols on the Ice Cloud Properties Over the Tibetan Plateau, J. Geophys. Res.-Atmos., 124, 9594-9608, https://doi.org/10.1029/2019JD030463, 2019.
Luo, L., Bai, X., Liu, S., Wu, B., Liu, W., Lv, Y., Guo, Z., Lin, S., Zhao, S., Hao, Y., Hao, J., Zhang, K., Zheng, A., and Tian, H.: Fine particulate matter ($PM_{2.5}$/PM_{10}) in Beijing, China: Variations and chemical compositions as well as sources, J. Environ. Sci., 121, 187-198, https://doi.org/10.1016/j.jes.2021.12.014, 2022.
Luo, Y., Zhou, X., Zhang, J., Xue, L., Chen, T., Zheng, P., Sun, J., Yan, X., Han, G., and Wang, W.: Characteristics of airborne water-soluble organic carbon (WSOC) at a background site of the North China Plain, Atmos. Res., 231, https://doi.org/10.1016/j.atmosres.2019.104668, 2020.
Ma, L., Li, B., Yabo, S. D., Li, Z., and Qi, H.: Fluorescence fingerprinting characteristics of water-soluble organic carbon from size-resolved particles during pollution event, Chemosphere, 307, https://doi.org/10.1016/j.chemosphere.2022.135748, 2022.
Ma, Y., Cheng, Y., Qiu, X., Cao, G., Fang, Y., Wang, J., Zhu, T., Yu, J., and Hu, D.: Sources and oxidative potential of water-soluble humic-like substances ($HULIS_{WS}$) in fine particulate matter ($PM_{2.5}$)

in Beijing, Atmos Chem Phys, 18, 5607-5617, https://doi.org/10.5194/acp-18-5607-2018, 2018.

Murphy, K. R., Stedmon, C. A., Graeber, D., and Bro, R.: Fluorescence spectroscopy and multi-way techniques. PARAFAC, Anal. Methods, 5, 6557-6566, https://doi.org/10.1039/C3AY41160E, 2013.

Murphy, K. R., Butler, K. D., Spencer, R. G. M., Stedmon, C. A., Boehme, J. R., and Aiken, G. R.: Measurement of Dissolved Organic Matter Fluorescence in Aquatic Environments: An Interlaboratory Comparison, Environ. Sci. Technol., 44, 9405-9412, https://doi.org/10.1021/es102362t, 2010.

Ng, N. L., Canagaratna, M. R., Jimenez, J. L., Chhabra, P. S., Seinfeld, J. H., and Worsnop, D. R.: Changes in organic aerosol composition with aging inferred from aerosol mass spectra, Atmos Chem Phys, 11, 6465-6474, https://doi.org/10.5194/acp-11-6465-2011, 2011.

Ng, N. L., Canagaratna, M. R., Zhang, Q., Jimenez, J. L., Tian, J., Ulbrich, I. M., Kroll, J. H., Docherty, K. S., Chhabra, P. S., Bahreini, R., Murphy, S. M., Seinfeld, J. H., Hildebrandt, L., Donahue, N. M., DeCarlo, P. F., Lanz, V. A., Prévôt, A. S. H., Dinar, E., Rudich, Y., and Worsnop, D. R.: Organic aerosol components observed in Northern Hemispheric datasets from Aerosol Mass Spectrometry, Atmos Chem Phys, 10, 4625-4641, https://doi.org/10.5194/acp-10-4625-2010, 2010.

Qi, P., Guo, X., Chang, Y., Tang, J., and Li, S.: Cloud water path, precipitation amount, and precipitation efficiency derived from multiple datasets on the Qilian Mountains, Northeastern Tibetan Plateau, Atmos. Res., 274, https://doi.org/10.1016/j.atmosres.2022.106204, 2022.

Saleh, R.: From Measurements to Models: Toward Accurate Representation of Brown Carbon in Climate Calculations, Curr. Pollut. Rep., 6, 90-104, https://doi.org/10.1007/s40726-020-00139-3, 2020.

Schnitzler, E. G. and Abbatt, J. P. D.: Heterogeneous OH oxidation of secondary brown carbon aerosol, Atmos Chem Phys, 18, 14539-14553, https://doi.org/10.5194/acp-18-14539-2018, 2018.

Schnitzler, E. G., Gerrebos, N. G. A., Carter, T. S., Huang, Y., Heald, C. L., Bertram, A. K., and Abbatt, J. P. D.: Rate of atmospheric brown carbon whitening governed by environmental conditions, Proc. Natl. Acad. Sci., 119, https://doi.org/10.1073/pnas.2205610119, 2022.

Siemens, K., Morales, A., He, Q., Li, C., Hettiyadura, A. P. S., Rudich, Y., and Laskin, A.: Molecular Analysis of Secondary Brown Carbon Produced from the Photooxidation of Naphthalene, Environ. Sci. Technol., 56, 3340-3353, https://doi.org/10.1021/acs.est.1c03135, 2022.

Stedmon, C. A. and Bro, R.: Characterizing dissolved organic matter fluorescence with parallel factor analysis: a tutorial, Limnol. Oceanogr.-Meth., 6, 572-579, https://doi.org/10.4319/lom.2008.6.572, 2008.

Stein, A. F., Draxler, R. R., Rolph, G. D., Stunder, B. J. B., Cohen, M. D., and Ngan, F.: Noaa's Hysplit Atmospheric Transport and Dispersion Modeling System, B. Am. Meteorol. Soc., 96, 2059-2077, https://doi.org/10.1175/BAMS-D-14-00110.1, 2015.

Sumlin, B. J., Pandey, A., Walker, M. J., Pattison, R. S., Williams, B. J., and Chakrabarty, R. K.: Atmospheric Photooxidation Diminishes Light Absorption by Primary Brown Carbon Aerosol from Biomass Burning, Environ. Sci. Tech. Let., 4, 540-545, https://doi.org/10.1021/acs.estlett.7b00393, 2017.

Tang, T., Huo, T., Tao, H., Tian, M., Yang, H., and Wang, H.: Effects of aerosol water content and acidity on the light absorption of atmospheric humic-like substances in winter, Chemosphere, 349, https://doi.org/10.1016/j.chemosphere.2023.140796, 2024.

Tao, Y., Yang, Z., Tan, X., Cheng, P., Wu, C., Li, M., Sun, Y., Ma, N., Dong, Y., Zhang, J., and Du, T.: Light Absorption Properties of Brown Carbon Aerosol During Winter at a Polluted Rural Site in the North China Plain, Atmosphere-Basel, 15, https://doi.org/10.3390/atmos15111294, 2024.

Ulbrich, I. M., Canagaratna, M. R., Zhang, Q., Worsnop, D. R., and Jimenez, J. L.: Interpretation of organic components from Positive Matrix Factorization of aerosol mass spectrometric data, Atmos Chem Phys, 9, 2891-2918, https://doi.org/10.5194/acp-9-2891-2009, 2009.

Wang, H., Su, Y., Liu, Y., Xie, F., Zhou, X., Yu, R., Lü, C., and He, J.: Water-soluble brown carbon in atmospheric aerosols from the resource-dependent cities: Optical properties, chemical compositions and sources, J. Environ. Sci., 138, 74-87, https://doi.org/10.1016/j.jes.2023.02.035, 2024.

Wang, Q., Han, Y., Ye, J., Liu, S., Pongpiachan, S., Zhang, N., Han, Y., Tian, J., Wu, C., Long, X., Zhang, Q., Zhang, W., Zhao, Z., and Cao, J.: High Contribution of Secondary Brown Carbon to Aerosol Light Absorption in the Southeastern Margin of Tibetan Plateau, Geophys. Res. Lett., 46, 4962-4970, https://doi.org/10.1029/2019GL082731, 2019.

Wen, H., Zhou, Y., Xu, X., Wang, T., Chen, Q., Chen, Q., Li, W., Wang, Z., Huang, Z., Zhou, T., Shi, J., Bi, J., Ji, M., and Wang, X.: Water-soluble brown carbon in atmospheric aerosols along the transport pathway of Asian dust: Optical properties, chemical compositions, and potential sources, Sci. Total. Environ., 789, https://doi.org/10.1016/j.scitotenv.2021.147971, 2021.

Wu, G., Fu, P., Ram, K., Song, J., Chen, Q., Kawamura, K., Wan, X., Kang, S., Wang, X., Laskin, A., and Cong, Z.: Fluorescence characteristics of water-soluble organic carbon in atmospheric aerosol, Environ. Pollut., 268, https://doi.org/10.1016/j.envpol.2020.115906, 2021.

Wu, G., Wan, X., Ram, K., Li, P., Liu, B., Yin, Y., Fu, P., Loewen, M., Gao, S., Kang, S., Kawamura, K., Wang, Y., and Cong, Z.: Light absorption, fluorescence properties and sources of brown carbon aerosols in the Southeast Tibetan Plateau, Environ. Pollut., 257, https://doi.org/10.1016/j.envpol.2019.113616, 2020.

Wu, G., Ram, K., Fu, P., Wang, W., Zhang, Y., Liu, X., Stone, E. A., Pradhan, B. B., Dangol, P. M., Panday, A. K., Wan, X., Bai, Z., Kang, S., Zhang, Q., and Cong, Z.: Water-Soluble Brown Carbon in Atmospheric Aerosols from Godavari (Nepal), a Regional Representative of South Asia, Environ. Sci. Technol., 53, 3471-3479, https://doi.org/10.1021/acs.est.9b00596, 2019.

Xie, F., Lin, Y., Ren, L., Gul, C., Wang, J., Cao, F., Zhang, Y., Xie, T., Wu, J., and Zhang, Y.: Decrease of atmospheric black carbon and CO concentrations due to COVID-19 lockdown at the Mt. Waliguan WMO/GAW baseline station in China, Environ. Res., 211, https://doi.org/10.1016/j.envres.2022.112984, 2022.

Xu, J., Hettiyadura, A. P. S., Liu, Y., Zhang, X., Kang, S., and Laskin, A.: Regional Differences of Chemical Composition and Optical Properties of Aerosols in the Tibetan Plateau, J. Geophys. Res.-Atmos., 125, https://doi.org/10.1029/2019JD031226, 2020a.

Xu, J., Hettiyadura, A. P. S., Liu, Y., Zhang, X., Kang, S., and Laskin, A.: Atmospheric Brown Carbon on the Tibetan Plateau: Regional Differences in Chemical Composition and Light Absorption Properties, Environ. Sci. Tech. Let., 9, 219-225, https://doi.org/10.1021/acs.estlett.2c00016, 2022.

Xu, J., Wang, Z., Yu, G., Qin, X., Ren, J., and Qin, D.: Characteristics of water soluble ionic species in fine particles from a high altitude site on the northern boundary of Tibetan Plateau: Mixture of mineral dust and anthropogenic aerosol, Atmos. Res., 143, 43-56,

https://doi.org/10.1016/j.atmosres.2014.01.018, 2014.
Xu, J., Zhang, Q., Wang, Z., Yu, G., Ge, X., and Qin, X.: Chemical composition and size distribution of summertime $PM_{2.5}$ at a high altitude remote location in the northeast of the Qinghai–Xizang (Tibet) Plateau: insights into aerosol sources and processing in free troposphere, Atmos Chem Phys, 15, 5069-5081, https://doi.org/10.5194/acp-15-5069-2015, 2015.
Xu, J., Mei, F., Zhang, X., Zhao, W., Zhai, L., Zhong, M., and Hou, S.: Impact of Anthropogenic Aerosol Transport on Cloud Condensation Nuclei Activity During Summertime in Qilian Mountain, in the Northern Tibetan Plateau, J. Geophys. Res.-Atmos., 129, https://doi.org/10.1029/2023JD040519, 2024a.
Xu, J., Wang, Z., Yu, G., Sun, W., Qin, X., Ren, J., and Qin, D.: Seasonal and diurnal variations in aerosol concentrations at a high-altitude site on the northern boundary of Qinghai-Xizang Plateau, Atmos. Res., 120, 240-248, https://doi.org/10.1016/j.atmosres.2012.08.022, 2013.
Xu, J., Tian, Y., Cheng, C., Wang, C., Lin, Q., Li, M., Wang, X., and Shi, G.: Characteristics and source apportionment of ambient single particles in Tianjin, China: The close association between oxalic acid and biomass burning, Atmos. Res., 237, https://doi.org/10.1016/j.atmosres.2020.104843, 2020b.
Xu, J., Zhang, Q., Shi, J., Ge, X., Xie, C., Wang, J., Kang, S., Zhang, R., and Wang, Y.: Chemical characteristics of submicron particles at the central Tibetan Plateau: insights from aerosol mass spectrometry, Atmos Chem Phys, 18, 427-443, https://doi.org/10.5194/acp-18-427-2018, 2018.
Xu, J., Zhang, X., Zhao, W., Zhai, L., Zhong, M., Shi, J., Sun, J., Liu, Y., Xie, C., Tan, Y., Li, K., Ge, X., Zhang, Q., and Kang, S.: High-resolution physicochemical dataset of atmospheric aerosols over the Tibetan Plateau and its surroundings, Earth Syst. Sci. Data, 16, 1875-1900, https://doi.org/10.5194/essd-16-1875-2024, 2024b.
Yan, J., Wang, X., Gong, P., Wang, C., and Cong, Z.: Review of brown carbon aerosols: Recent progress and perspectives, Sci. Total. Environ., 634, 1475-1485, https://doi.org/10.1016/j.scitotenv.2018.04.083, 2018.
Yang, F., Chen, H., Wang, X., Yang, X., Du, J., and Chen, J.: Single particle mass spectrometry of oxalic acid in ambient aerosols in Shanghai: Mixing state and formation mechanism, Atmos. Environ., 43, 3876-3882, https://doi.org/10.1016/j.atmosenv.2009.05.002, 2009.
Yang, Y., Qin, J., Qi, T., Zhou, X., Chen, R., Tan, J., Xiao, K., Ji, D., He, K., and Chen, X.: Fluorescence characteristics of particulate water-soluble organic compounds emitted from coal-fired boilers, Atmos. Environ., 223, https://doi.org/10.1016/j.atmosenv.2020.117297, 2020.
Yu, F., Li, X., Zhang, R., Guo, J., Yang, W., Tripathee, L., Liu, L., Wang, Y., Kang, S., and Cao, J.: Insights into dissolved organics in non-urban areas-Optical properties and sources, Environ. Pollut., 329, https://doi.org/10.1016/j.envpol.2023.121641, 2023.
Yu, L., Zhang, M., Wang, L., Qin, W., Jiang, D., and Li, J.: Variability of surface solar radiation under clear skies over Qinghai-Tibet Plateau: Role of aerosols and water vapor, Atmos. Environ., 287, https://doi.org/10.1016/j.atmosenv.2022.119286, 2022.
Zhai, L., An, Y., Feng, L., Qin, X., and Xu, J.: Contrasting the physical and chemical characteristics of dissolved organic matter between glacier and glacial runoff from a mountain glacier on the Tibetan Plateau, Sci. Total. Environ., 848, https://doi.org/10.1016/j.scitotenv.2022.157784, 2022.
Zhang, C., Chen, M., Kang, S., Yan, F., Han, X., Gautam, S., Hu, Z., Zheng, H., Chen, P., Gao, S., Wang, P., and Li, C.: Light absorption and fluorescence characteristics of water-soluble organic

compounds in carbonaceous particles at a typical remote site in the southeastern Himalayas and Tibetan Plateau, Environ. Pollut., 272, https://doi.org/10.1016/j.envpol.2020.116000, 2021a.

Zhang, X., Xu, J., and Kang, S.: Chemical characterization of submicron particulate matter (PM_1) emitted by burning highland barley in the northeastern part of the Qinghai-Tibet Plateau, Atmos. Environ., 224, https://doi.org/10.1016/j.atmosenv.2020.117351, 2020.

Zhang, X., Xu, J., Kang, S., Zhang, Q., and Sun, J.: Chemical characterization and sources of submicron aerosols in the northeastern Qinghai-Tibet Plateau: insights from high-resolution mass spectrometry, Atmos Chem Phys, 19, 7897-7911, https://doi.org/10.5194/acp-19-7897-2019, 2019.

Zhang, X., Xu, J., Kang, S., Sun, J., Shi, J., Gong, C., Sun, X., Du, H., Ge, X., and Zhang, Q.: Regional Differences in the Light Absorption Properties of Fine Particulate Matter Over the Tibetan Plateau: Insights From HR-ToF-AMS and Aethalometer Measurements, J. Geophys. Res.-Atmos., 126, https://doi.org/10.1029/2021JD035562, 2021b.

Zhang, Y., Xu, J., Shi, J., Xie, C., Ge, X., Wang, J., Kang, S., and Zhang, Q.: Light absorption by water-soluble organic carbon in atmospheric fine particles in the central Tibetan Plateau, Environ. Sci. Pollut. R., 24, 21386-21397, https://doi.org/10.1007/s11356-017-9688-8, ~~2017~~2017a.

Zhang, Y., Forrister, H., Liu, J., Dibb, J., Anderson, B., Schwarz, J. P., Perring, A. E., Jimenez, J. L., Campuzano-Jost, P., Wang, Y., Nenes, A., and Weber, R. J.: Top-of-atmosphere radiative forcing affected by brown carbon in the upper troposphere, Nature Geosci., 10, 486-+, https://doi.org/10.1038/ngeo2960, 2017b.

Zhao, S., Ming, J., Xiao, C., Sun, W., and Qin, X.: A preliminary study on measurements of black carbon in the atmosphere of northwest Qilian Shan, J. Environ. Sci., 24, 152-159, https://doi.org/10.1016/S1001-0742(11)60739-0, 2012.

Zhao, W., Zhang, X., Zhai, L., Shen, X., and Xu, J.: Chemical characterization and sources of submicron aerosols in Lhasa on the Qinghai-Tibet Plateau: Insights from high-resolution mass spectrometry, Sci. Total. Environ., 815, 152866, https://doi.org/10.1016/j.scitotenv.2021.152866, 2022.

Zheng, X., Shen, C., Wan, G., Tang, J., and Liu, K.: Mass and isotopic concentrations of water-insoluble refractory carbon in total suspended particulates at Mt. Waliguan Observatory (China), Particuology, 20, 24-31, https://doi.org/10.1016/j.partic.2014.11.003, 2015.

Zheng, Z., Zhu, W., Chen, G., Jiang, N., Fan, D., and Zhang, D.: Continuous but diverse advancement of spring-summer phenology in response to climate warming across the Qinghai-Tibetan Plateau, Agr. Forest Meteorol., 223, 194-202, https://doi.org/10.1016/j.agrformet.2016.04.012, 2016.

Zhong, M., Xu, J., Wang, H., Gao, L., Zhu, H., Zhai, L., Zhang, X., and Zhao, W.: Characterizing water-soluble brown carbon in fine particles in four typical cities in northwestern China during wintertime: integrating optical properties with chemical processes, Atmos Chem Phys, 23, 12609-12630, https://doi.org/10.5194/acp-23-12609-2023, 2023.

Zhu, C., Qu, Y., Huang, H., Chen, J., Dai, W., Huang, R., and Cao, J.: Black Carbon and Secondary Brown Carbon, the Dominant Light Absorption and Direct Radiative Forcing Contributors of the Atmospheric Aerosols Over the Tibetan Plateau, Geophys. Res. Lett., 48, https://doi.org/10.1029/2021GL092524, 2021.

Zhu, C., Qu, Y., Huang, H., Shi, J., Dai, W., Zhang, N., Wang, N., Wang, L., Ji, S., and Cao, J.: Brown Carbon From Biomass Burning Reinforces the Himalayas and Tibetan Plateau Warming,

Geophys. Res. Lett., 51, https://doi.org/10.1029/2023GL107269, 2024.

Zsolnay, A., Baigar, E., Jimenez, M., Steinweg, B., and Saccomandi, F.: Differentiating with fluorescence spectroscopy the sources of dissolved organic matter in soils subjected to drying, Chemosphere, 38, 45-50, https://doi.org/10.1016/S0045-6535(98)00166-0, 1999.

Figure

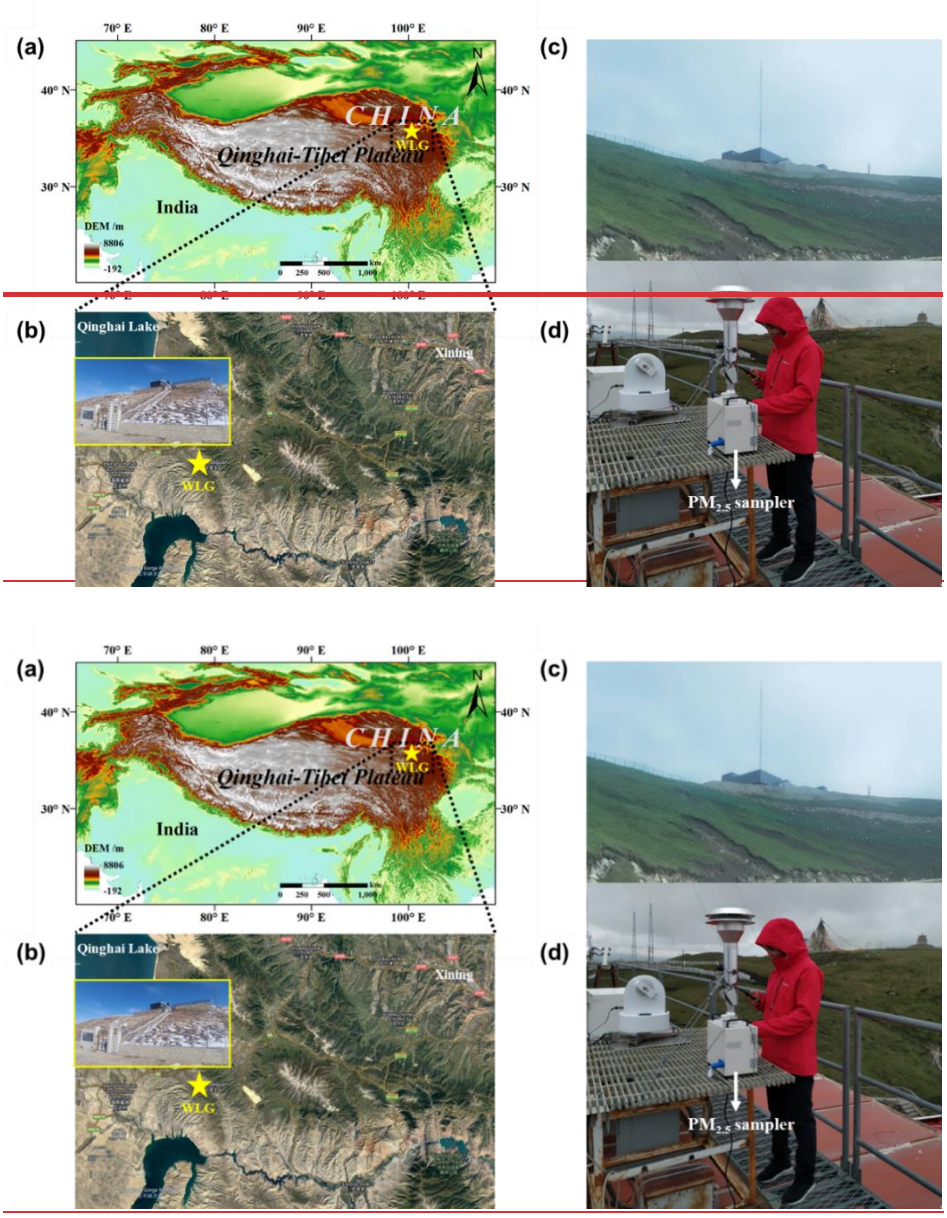

Figure 1. (a, b) Location ~~map~~ of the Waliguan Baseline Observatory (WLG) on the Tibetan Plateau (TP~~, (b) and~~), adapted from Zhao et al. (2022) (© Google Maps 2025). (c~~) images~~, d) Photographs of ~~Waliguan Baseline Observatory and other surrounding areas, and (d)~~ the WLG and *in-situ* $PM_{2.5}$ sampling.

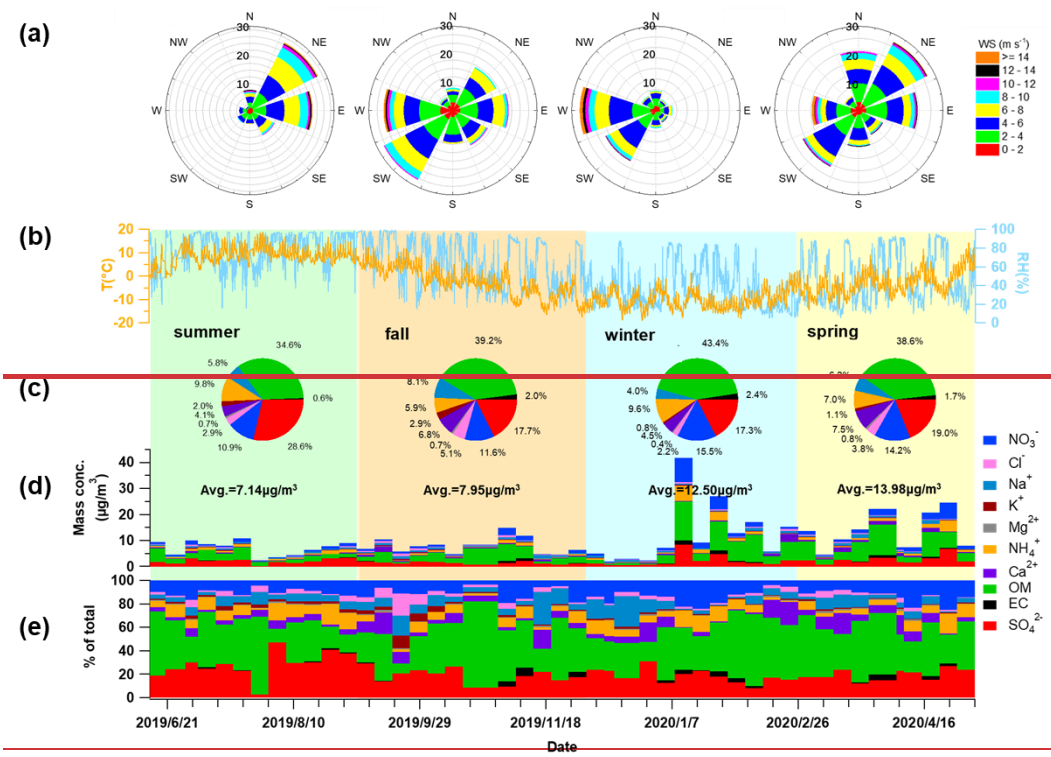
(a)
(b)
(c)
(d)
(e)
WS (m s-1)
>= 14
12 - 14
10 - 12
8 - 10
6 - 8
4 - 6
2 - 4
0 - 2
T(°C)
RH(%)
summer
fall
winter
spring
34.6%
5.8%
9.8%
0.6%
2.0%
4.1%
0.7%
2.9%
10.9%
28.6%
39.2%
8.1%
2.0%
5.9%
2.9%
6.8%
0.7%
5.1%
11.6%
17.7%
43.4%
4.0%
2.4%
9.6%
0.8%
4.5%
0.4%
2.2%
15.5%
17.3%
38.6%
7.0%
1.7%
1.1%
7.5%
0.8%
3.8%
14.2%
19.0%
Mass conc. (μg/m3)
Avg.=7.14μg/m3
Avg.=7.95μg/m3
Avg.=12.50μg/m3
Avg.=13.98μg/m3
NO3-
Cl-
Na+
K+
Mg2+
NH4+
Ca2+
OM
EC
SO42-
% of total
2019/6/21
2019/8/10
2019/9/29
2019/11/18
2020/1/7
2020/2/26
2020/4/16
Date

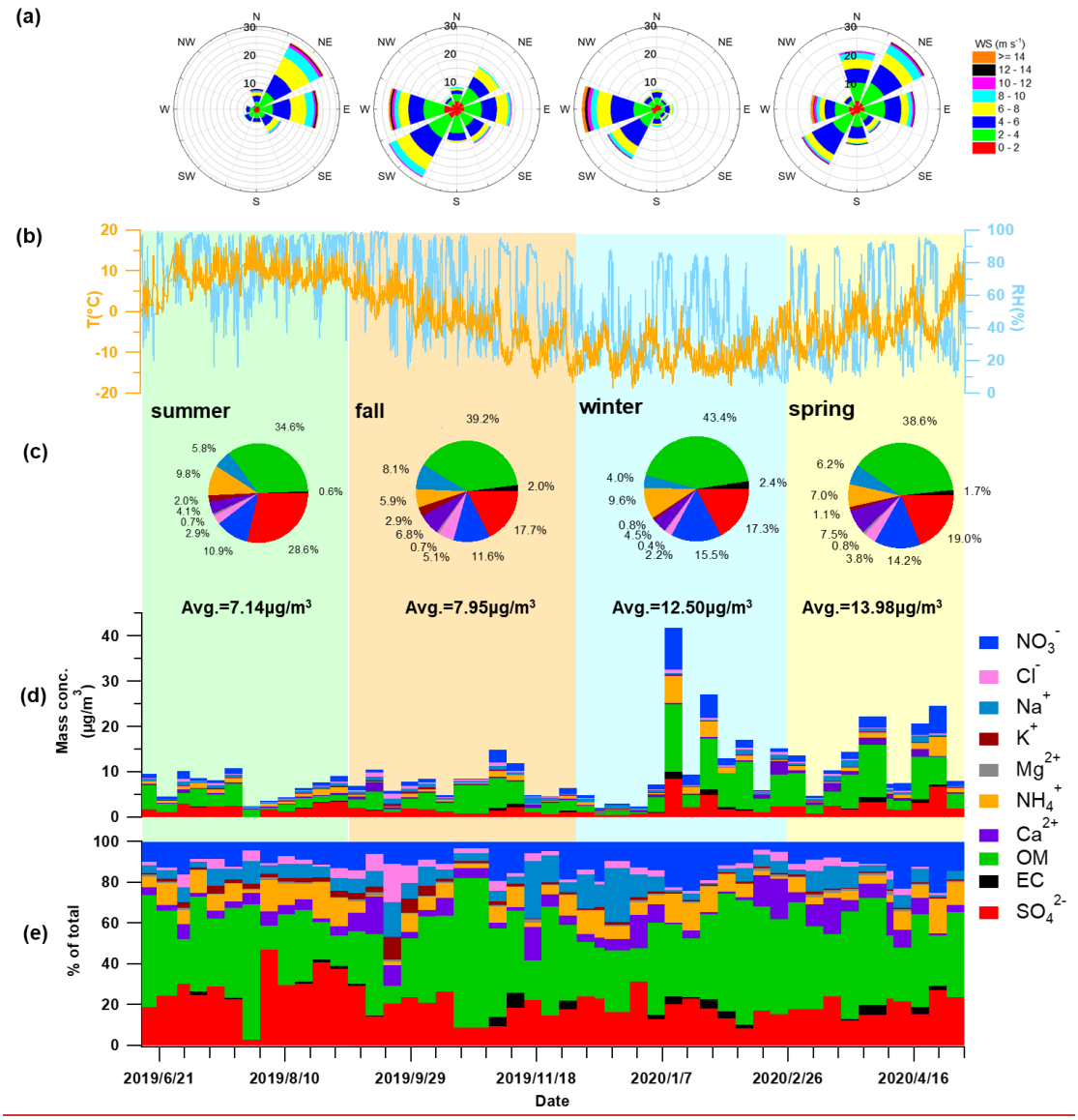

Figure 2. Overview of the dataset used in this study. (a) Wind-rose ~~diagram~~diagrams for ~~four seasons,~~each season; (b) time series of air temperature (T) and relative humidity (RH~~),~~); (c) seasonal average average chemical composition ~~for four seasons,~~; (d) mass concentration of all measured species, including water-soluble ions (WSIs ~~+ OM +~~), organic matter (OM), and elemental carbon (EC~~),~~); and (e) ~~percentage of~~ relative contributions of each species to the total $PM_{2.5}$ mass ~~concentration by species~~.

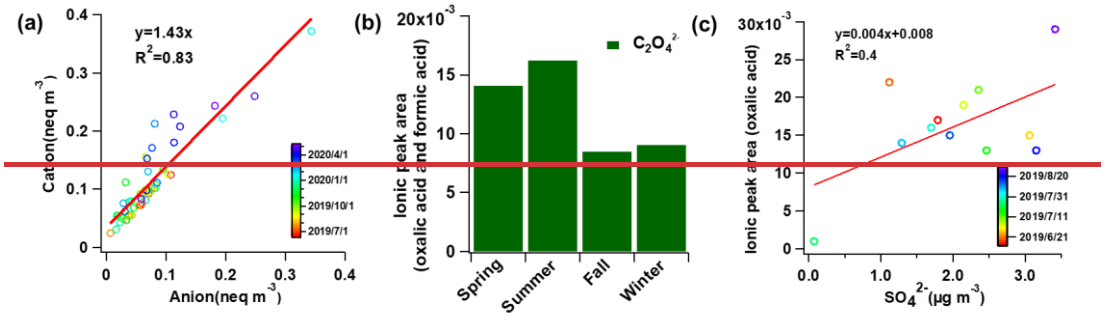

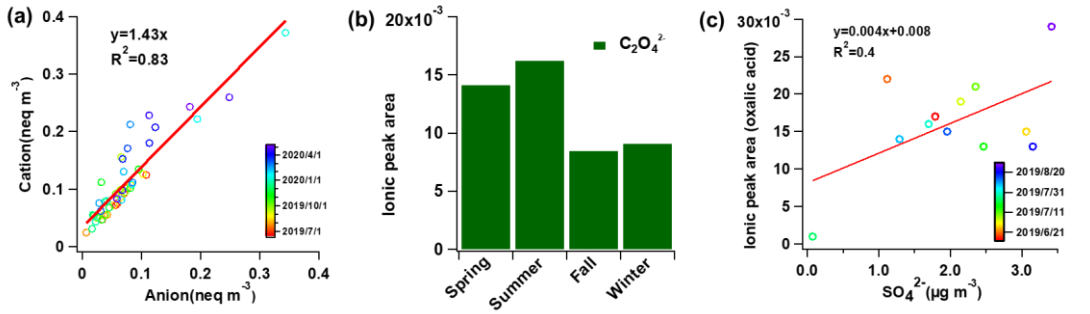

Figure 3. (a) ~~The charge~~Charge balance between ~~the~~major cations ($Na^+ + NH_4^+ + K^+ + Ca^{2+} + Mg^{2+}$) and anions ($Cl^- + NO_3^- + SO_4^{2-}$~~).~~); (b) ~~Ion peak areas~~seasonal variation of oxalic acid ~~for four seasons,~~ion peak areas; and (c) correlation between oxalate ion peak area and mass concentration of sulfate ~~during~~in summer. Two scatter plots are fitted with linear regression, the fitting equations and coefficients are shown in the figure.

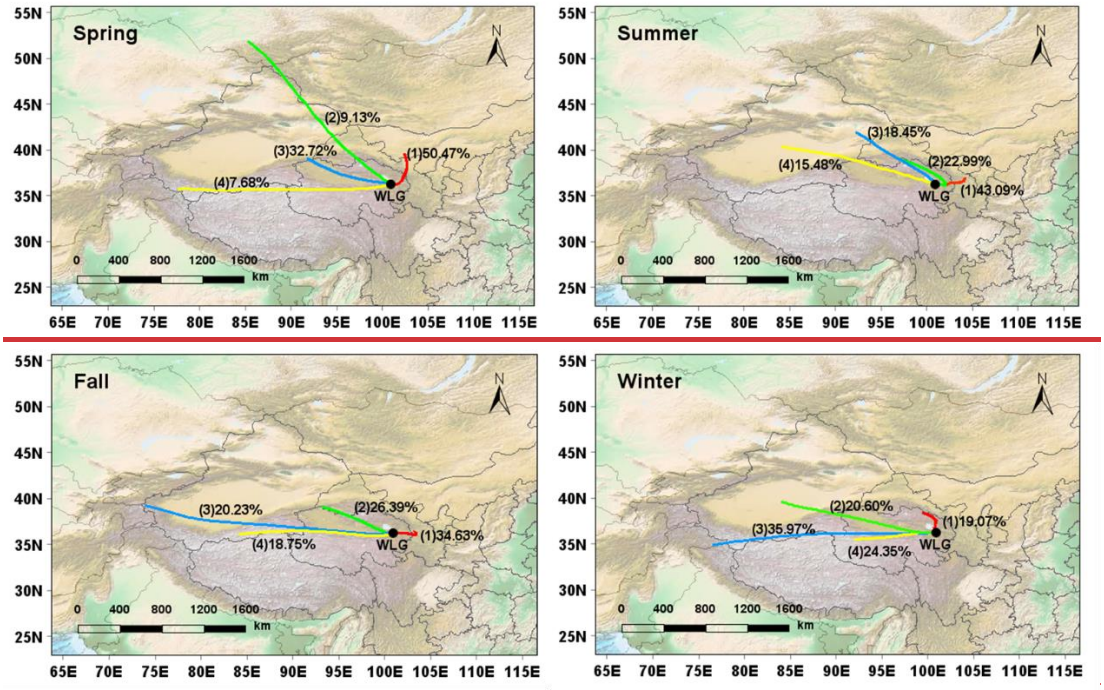

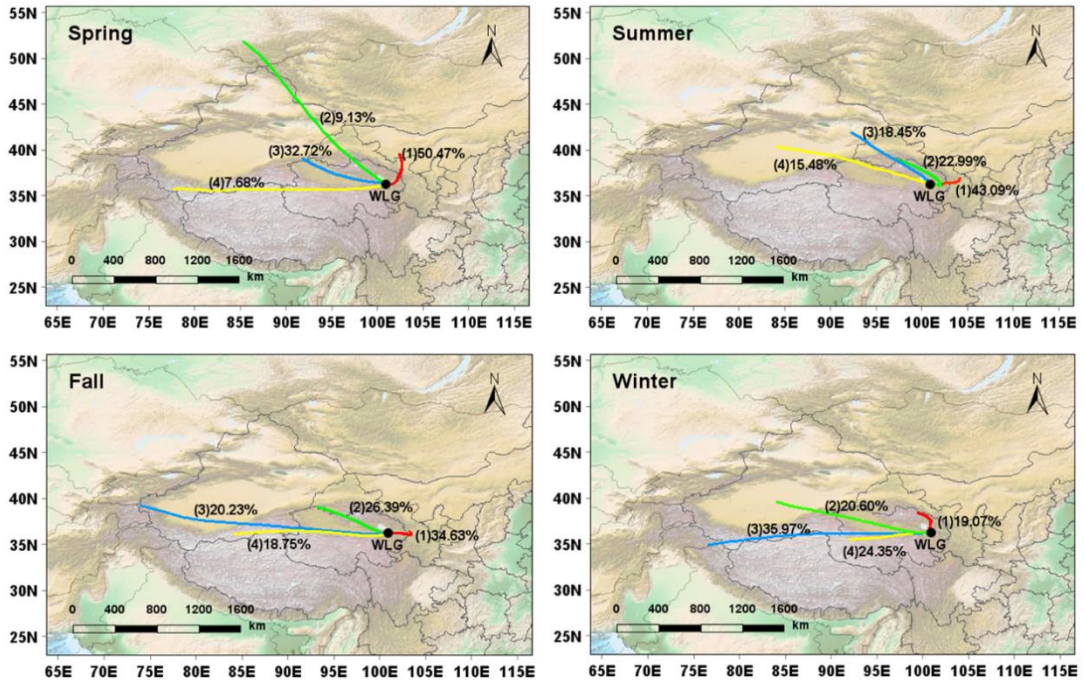

Figure 4 ~~The average backward trajectory clusters and percentage of air mass for the four seasons during the observation period.~~

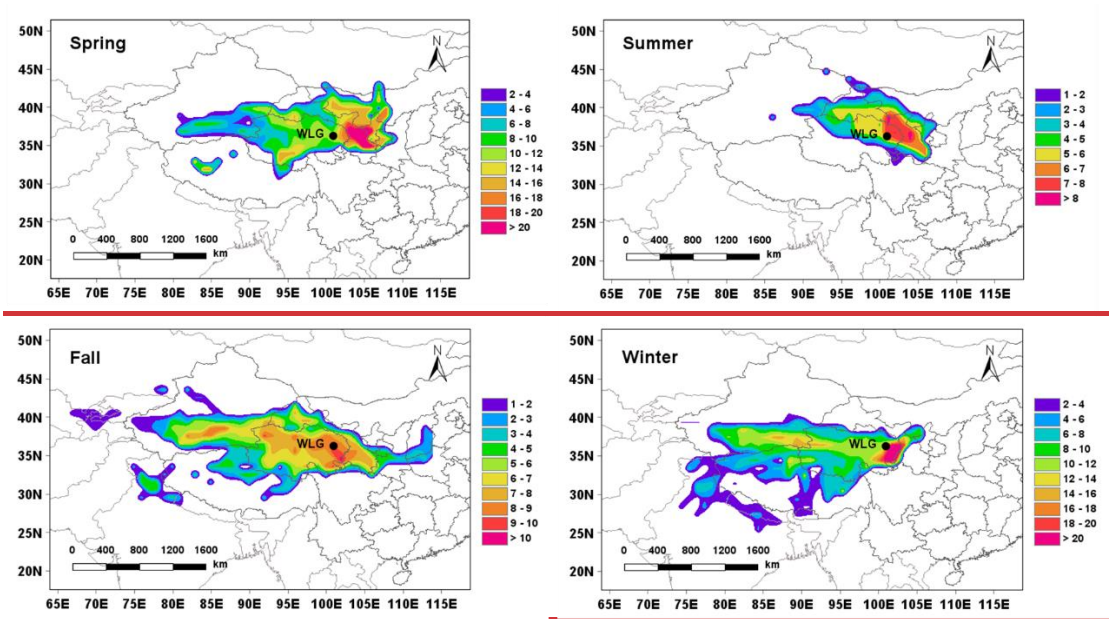

. Seasonal cluster analysis of 72-hour air mass backward trajectories arriving at the WLG at 500 m above the ground based on the GRADS dataset using HYSPLIT mode embedded in MeteoInfo software.

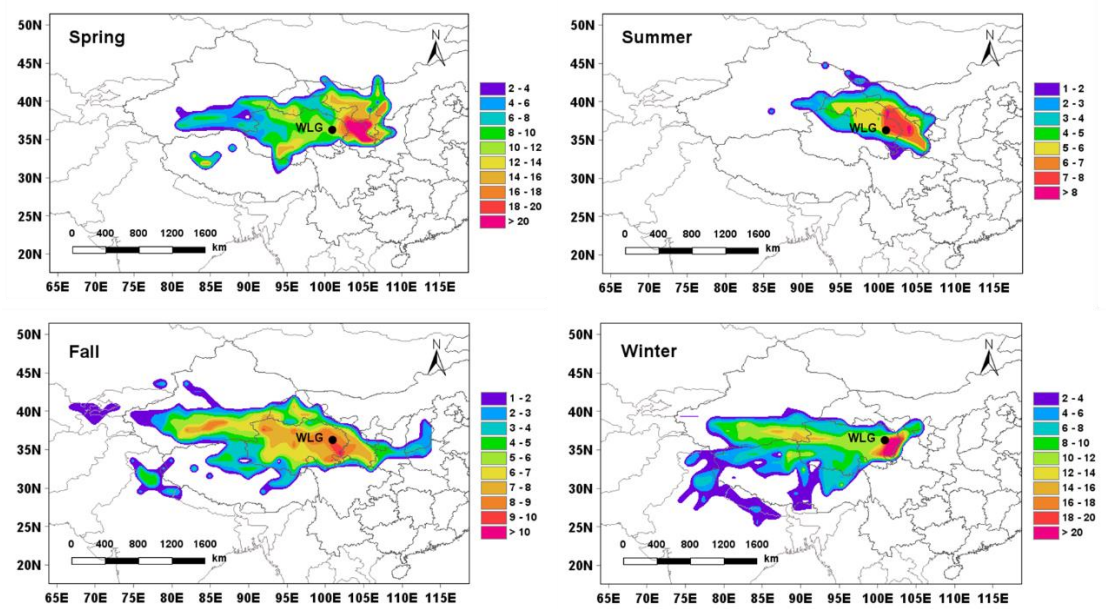

Figure 5–. Seasonal concentration-weighted trajectory (CWT) analysis of ~~WLG~~ $PM_{2.5}$ mass concentrations and air mass trajectories shown in ~~four seasons~~Figure 4 performed using MeteoInfor software.

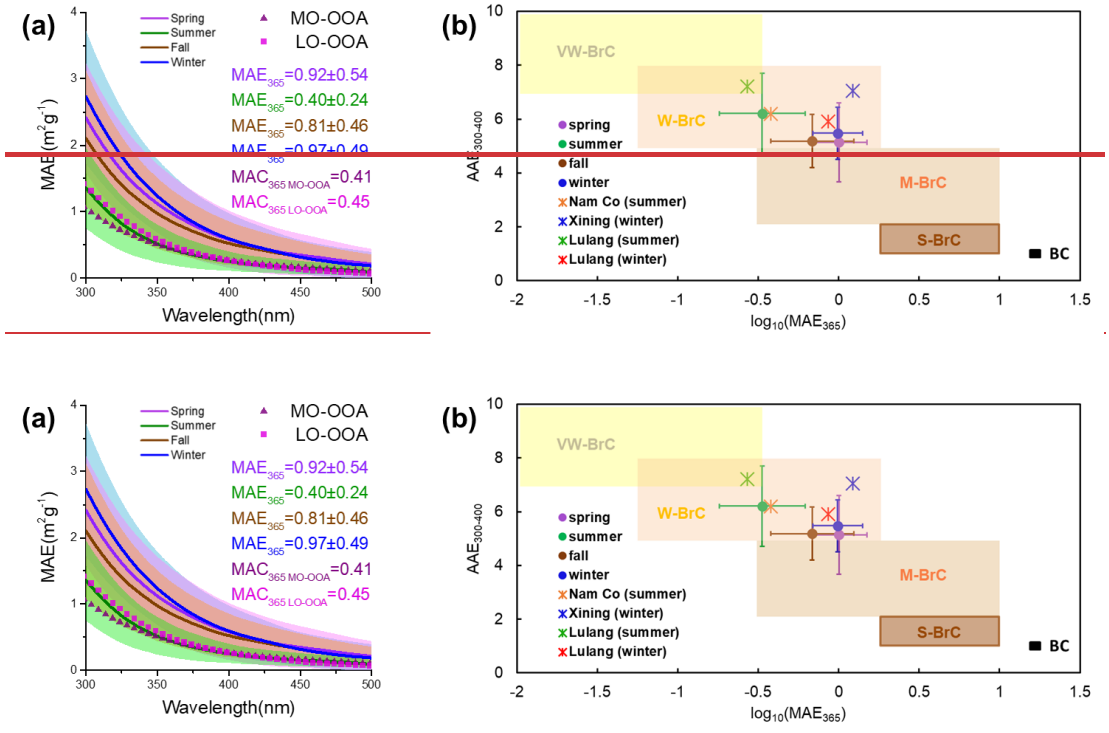

Figure 6. Optical properties of water-soluble BrC (WS-BrC) in different seasons. (a) ~~The average~~ Average mass absorption efficiency (MAE~~ spectrum~~) spectra and standard deviations of WS-BrC ~~in different seasons and~~ for each season, as well as for the two PMF-resolved factors ~~of WSOA analysed by PMF.~~(MO-OOA and LO-OOA). (b) Optical ~~based BrC~~ classification ~~map in~~of WS-BrC based on the AAE-~~$\log_{10}$MAE$_{365}$~~$\log_{10}$(MAE$_{365}$) framework proposed by Saleh (2020). The shaded

~~squares in the map~~regions from left to right represent “very weakly” (VW), “weakly” (W), “moderately” (M), and “strongly” (S) absorbing BrC classes, and black carbon (BC). The irregular marks ~~are different station~~indicate data from various TP ~~that have been~~sites reported ~~by other researchers before~~in previous studies.

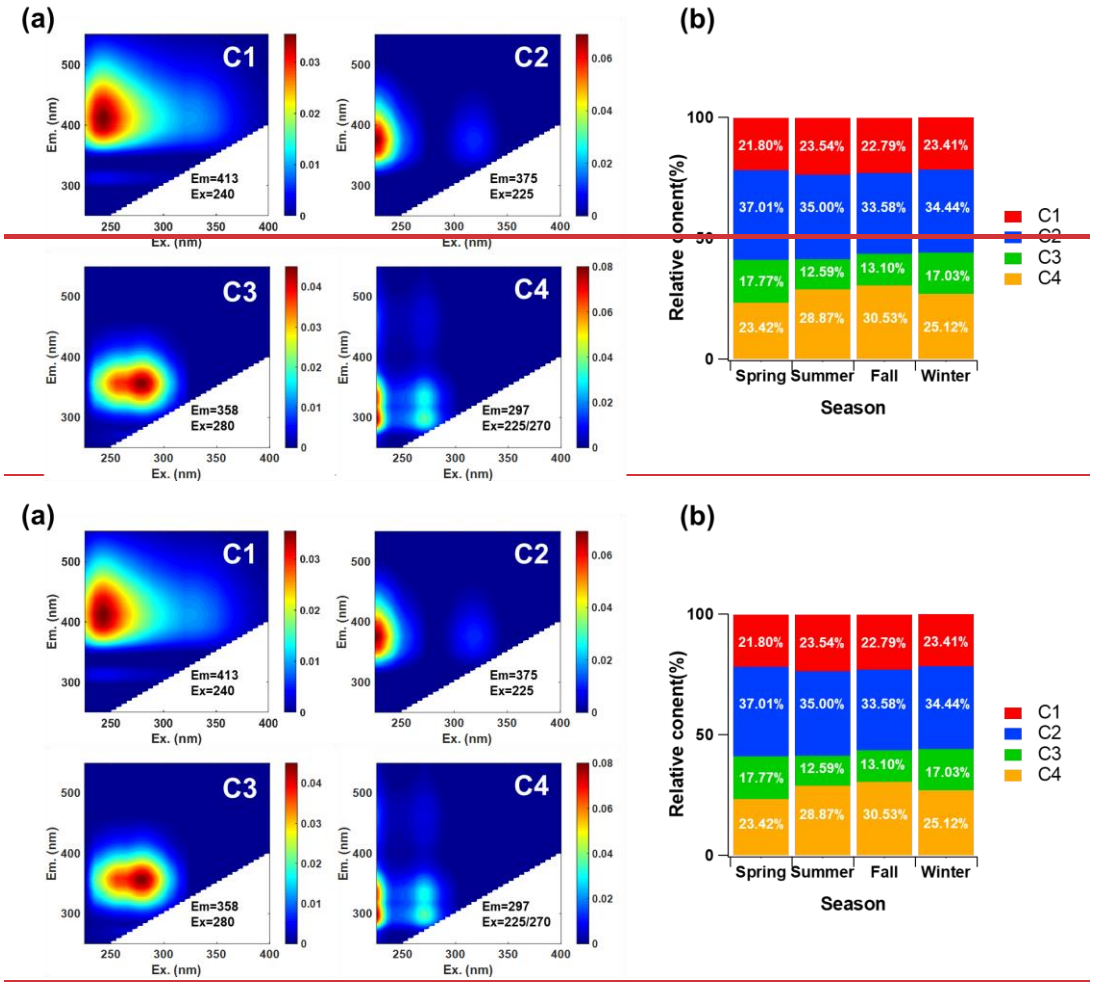

(a)
C1
Em=413
Ex=240
C2
Em=375
Ex=225
C3
Em=358
Ex=280
C4
Em=297
Ex=225/270
Em. (nm)
Ex. (nm)
(b)
Relative conent(%)
21.80%
23.54%
22.79%
23.41%
37.01%
35.00%
33.58%
34.44%
17.77%
12.59%
13.10%
17.03%
23.42%
28.87%
30.53%
25.12%
Spring
Summer
Fall
Winter
Season
C1
C2
C3
C4

Figure 7. Florescence analysis results. (a) Four excitation-emission matrix (EEM) components identified by the PARAFAC model for the water-soluble organic aerosol (WSOA ~~and~~); (b) seasonal variation in the relative ~~contribution percentage~~contributions of each component ~~in different seasons~~.

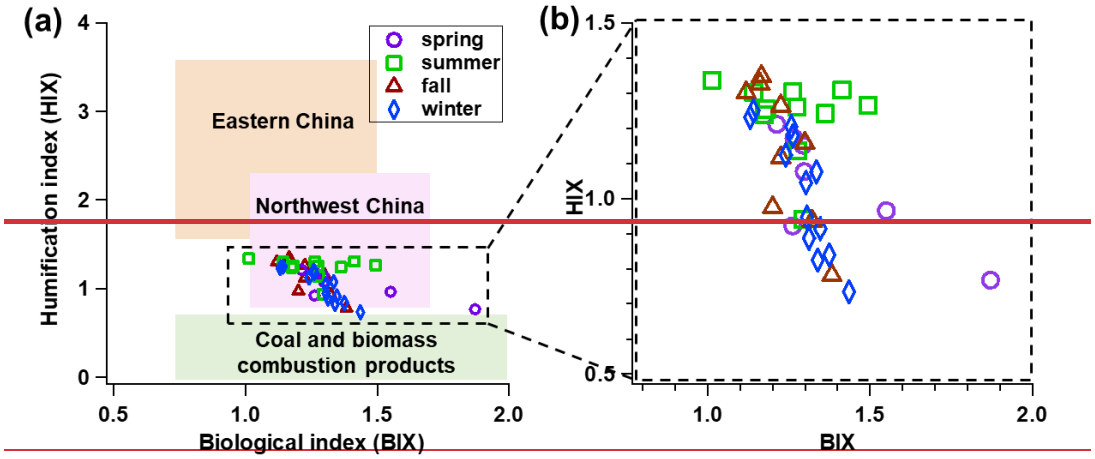

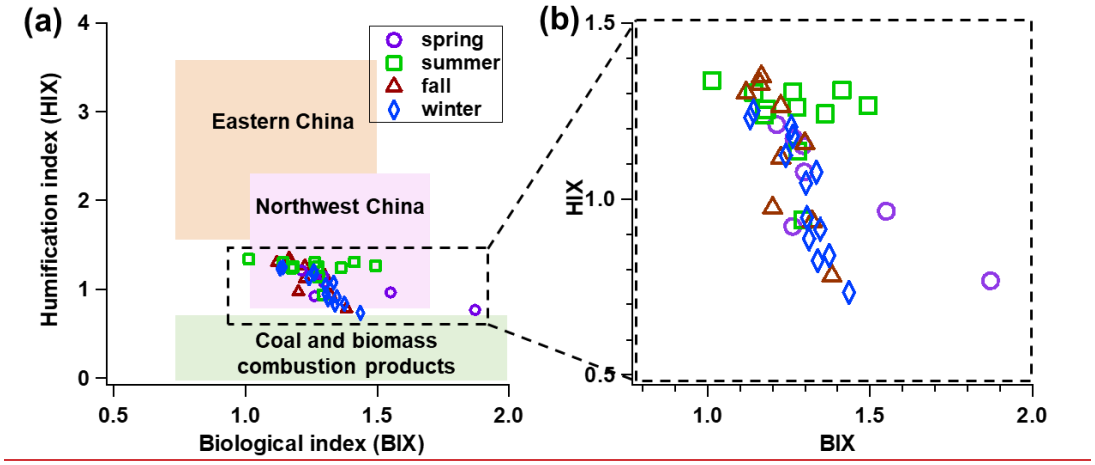

Figure 8. Characteristics of fluorescence results represented by the biological index (BIX) and humification index (HIX). (a) ~~and (b) BIX-HIX distribution map for four seasons, where orange, purple, and green boxes respectively represent the aerosol BIX-HIX range over~~Comparison of our dataset with previously reported values from eastern China, western China, and coal and biomass combustion ~~products~~sources, as summarized by Zhong et al. (2023)~~.~~; (b) enlarged view of our dataset highlighting seasonal variations.

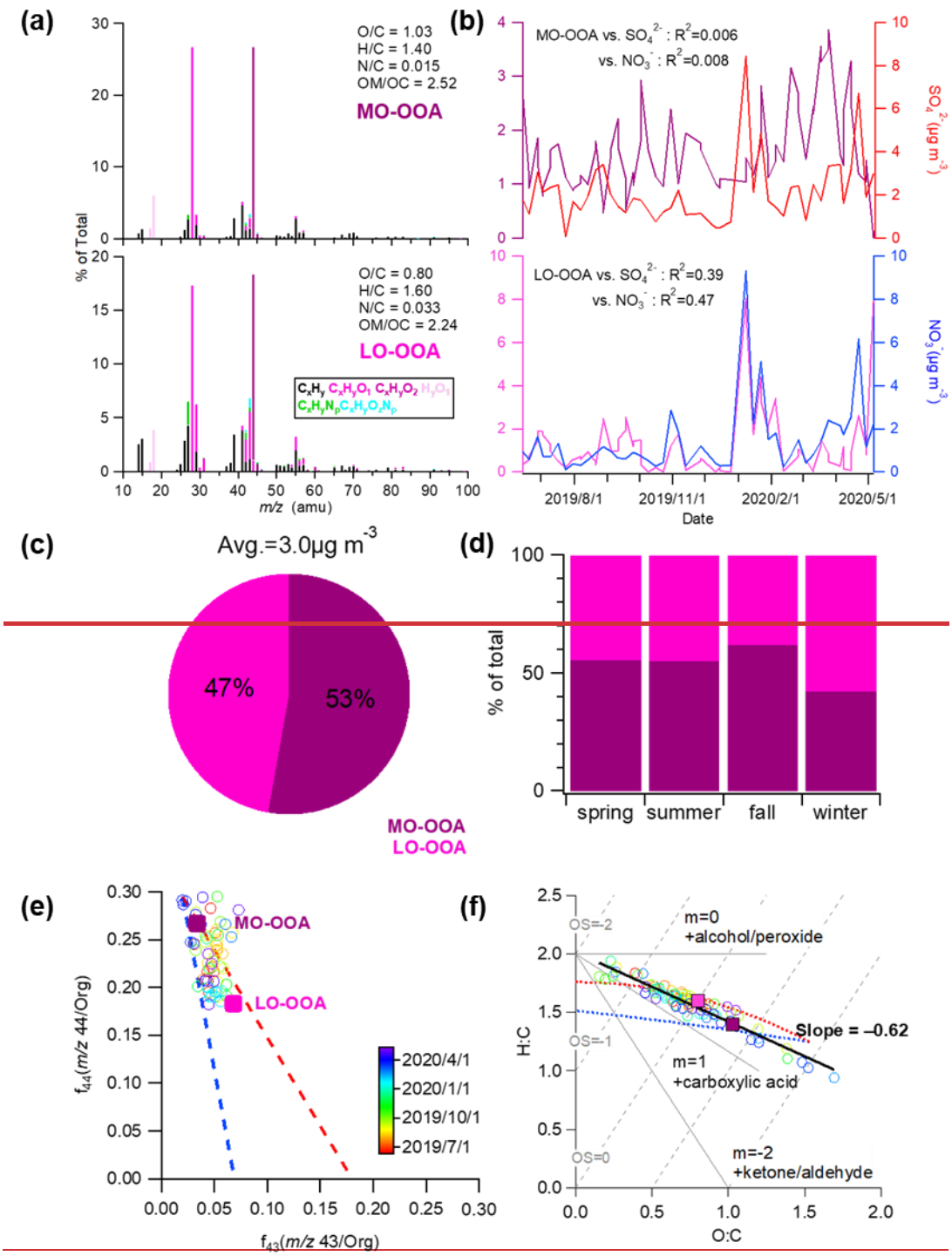
(a)
O/C = 1.03
H/C = 1.40
N/C = 0.015
OM/OC = 2.52
MO-OOA
O/C = 0.80
H/C = 1.60
N/C = 0.033
OM/OC = 2.24
LO-OOA
% of Total
m/z (amu)
(b)
MO-OOA vs. SO4 2- : R2=0.006
vs. NO3- : R2=0.008
LO-OOA vs. SO4 2- : R2=0.39
vs. NO3- : R2=0.47
SO4 2- (μg m-3)
NO3- (μg m-3)
2019/8/1
2019/11/1
2020/2/1
2020/5/1
Date
(c)
Avg.=3.0μg m-3
47%
53%
MO-OOA
LO-OOA
(d)
% of total
spring
summer
fall
winter
(e)
MO-OOA
LO-OOA
2020/4/1
2020/1/1
2019/10/1
2019/7/1
f44(m/z 44/Org)
f43(m/z 43/Org)
(f)
OS=-2
OS=-1
OS=0
m=0
+alcohol/peroxide
m=1
+carboxylic acid
m=-2
+ketone/aldehyde
Slope = –0.62
H:C
O:C

1061

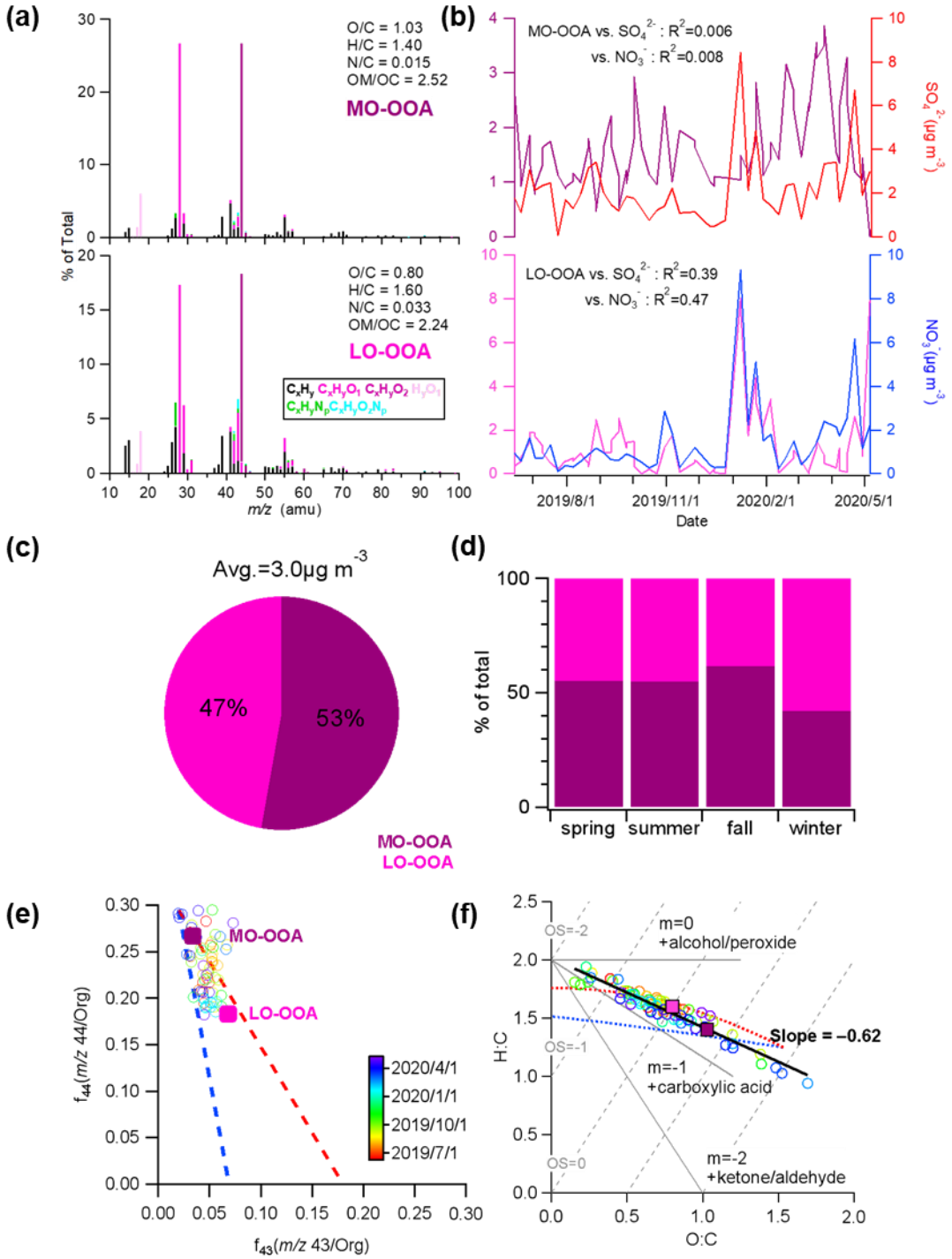

Figure 9. Offline HR-ToF-AMS analysis results. (a) PMF results of high-resolution mass spectra colored by six ion categories for the two OA factors at *m/z* < 120~~,~~; (b) ~~comparison of mass concentration~~ time series ~~changes~~of the mass concentrations of the two factors ~~with~~and their correlation ~~of~~with tracer species~~,~~; (c) ~~the~~ average contribution of ~~mass concentration of~~ each ~~factors~~factor to total ~~organics,~~organic mass concentration; (d) seasonal contributions of the ~~contribution percentage of~~ two factors to ~~the~~ total OA mass ~~in four seasons,~~; (e) ~~*f*44 vs. *f*43~~ triangle plot~~, and (f) the~~ of *f*44 vs. *f*43 for all the samples; (f) Van Krevelen diagram (H~~÷~~:C vs. O~~÷~~:C) for ~~the WLG samples and OA components, where the red and blue dashed lines correspond to the same color dashed lines in the *f*44 vs. *f*43 triangle plot~~all the samples.

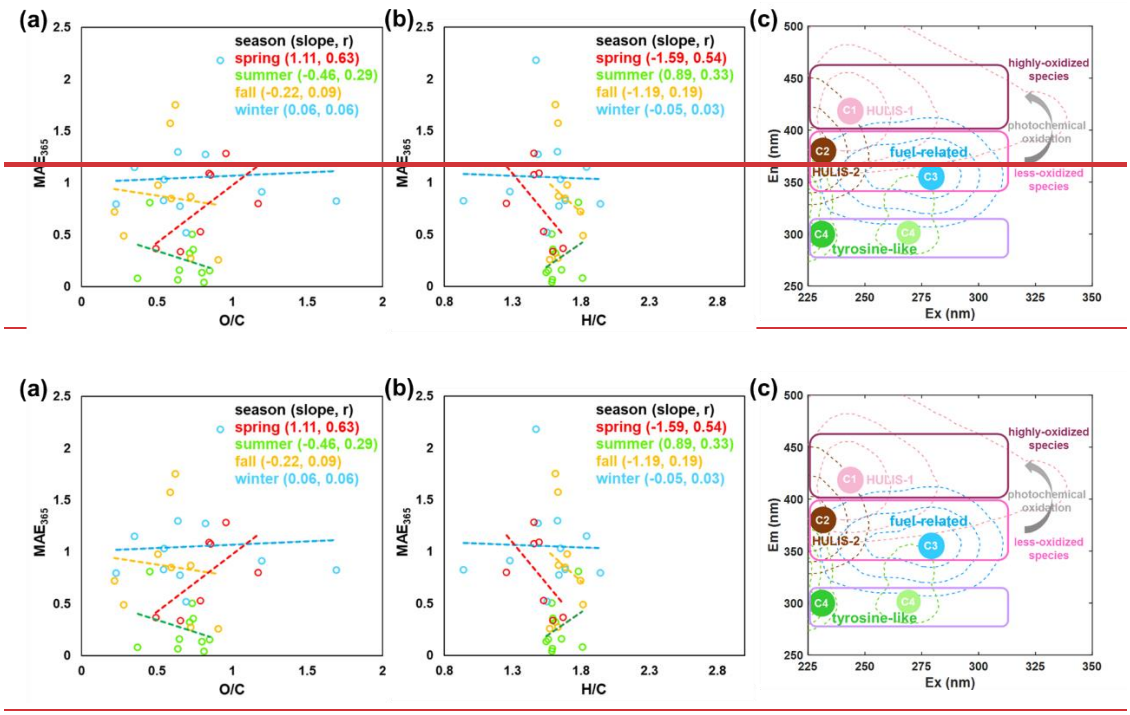

Figure 10~~ (a)~~. Relationships between optical properties and ~~(~~chemical characteristics. (a, b) ~~Scatterplot~~Scatterplots of MAE_{365} ~~with~~versus O/C and H/C ratios for the four seasons~~.~~; (c) ~~The position of~~ fluorescence peak positions of ~~chromophore~~chromophores and ~~corresponding oxidizing species.~~

their potential oxidation state.

Table

Table 1 Light-absorbing properties of BrC and fluorescence indices of WSOA ~~in~~across the four seasons.

Season	Abs_{365} (M/m)	$AAE_{300-400}$	MAE_{365} (m^2/g)	HIX	BIX
Spring	1.45 ± 0.54	5.14 ± 1.46	0.92 ± 0.54	1.04±0.16	1.39±0.24
Summer	0.36 ± 0.21	6.21 ± 1.50	0.40 ± 0.24	1.24±0.11	1.26±0.13
Fall	0.88 ± 0.70	5.19 ± 1.00	0.81 ± 0.46	1.13±0.20	1.23±0.09
Winter	1.55 ± 1.30	5.48 ± 0.96	0.97 ± 0.49	1.02±0.17	1.29±0.09